



TECHNISCHE UNIVERSITÄT MÜNCHEN

MASTER THESIS

**Production of $K^*(892)^+$ in p+p collisions
at 3.5 GeV**

Author:

Dimitar MIHAYLOV

Supervisors:

Prof. Dr. Laura FABBIETTI

Dr. Kirill LAPIDUS

*A thesis submitted in fulfilment of the requirements
for the degree of Master of Science*

in the

Physics Department

May, 2016

Declaration of Authorship

I, Dimitar MIHAYLOV, declare that this thesis titled, 'Production of $K^*(892)^+$ in p+p collisions at 3.5 GeV' and the work presented in it are my own. I confirm that:

- This work was done wholly or mainly while in candidature for a research degree at this University.
- Where any part of this thesis has previously been submitted for a degree or any other qualification at this University or any other institution, this has been clearly stated.
- Where I have consulted the published work of others, this is always clearly attributed.
- Where I have quoted from the work of others, the source is always given. With the exception of such quotations, this thesis is entirely my own work.
- I have acknowledged all main sources of help.
- Where the thesis is based on work done by myself jointly with others, I have made clear exactly what was done by others and what I have contributed myself.

Signed: Dimitar Mihaylov

Date: 3rd May, 2016

TECHNISCHE UNIVERSITÄT MÜNCHEN

Abstract

Physics Department

Master of Science

Production of $K^*(892)^+$ in p+p collisions at 3.5 GeV

by Dimitar MIHAYLOV

The **H**igh **A**cceptance **D**i-**E**lectron **S**pectrometer (HADES) is a fixed-target experiment located at the GSI Helmholtz Centre for Heavy Ion Research and operating at the SIS18 synchrotron, which provides energies of up to 2 GeV per nucleon. The HADES research program is focused on exploring the dense nuclear matter by means of di-electron spectroscopy. However, the detector is also suited for hadron detection. In April 2007 a proton beam with a kinetic energy of 3.5 GeV, which corresponds to $\sqrt{s} = 3.18$ GeV, was shot at a liquid hydrogen target. The data were really suitable for strangeness research, i.e. investigation of hadrons that contain a strange quark, and several studies were performed on this topic (e.g. [1–5]). The excited kaonic state $K^*(892)^+$ has a production threshold energy of 2.95 GeV, which is just a little bit below the available energy. The deep sub-threshold production of $K^*(892)^+$ has previously been measured by HADES in Ar+KCl reactions at beam energy of 1.756 GeV [1]. There are also measurements of this particle species at high energies, however no previous detection of $K^*(892)^+$ has been recorded at threshold energies. This inspired the investigation of this particular type of particle. The following work explains the method used for extraction of the total production cross section of $K^*(892)^+$ in 3.5 GeV p+p collisions and discusses the measurement of its spin-alignment properties. The results can be greatly beneficial to the current transport models and can complement further results from future experiments at HADES, when the detector will be moved to the newly developed **F**acility for **A**ntiproton and **I**on **R**esearch (FAIR) and will be provided with higher beam energies. Furthermore the results can be used as a reference for analyses of heavy-ion reactions at similar beam energies. Such data, collected during the 2008 p+Nb beam time at a kinetic energy of 3.5 GeV, are already available from HADES. This work was performed within the framework of my master studies and inspired a paper published in 2015 [6].

Acknowledgements

The story of my study is one probably just as dramatic, interesting and exciting as any modern problem in physics. I had a lot of ups and downs during both my Bachelor and Master studies, but there was one very important and fundamental constant - the support I got from the people around me. I want to express special thanks to Prof. Dr. Laura Fabbietti for providing me with the opportunity to work in such a fantastic environment and to my direct supervisor Dr. Kirill Lapidus, not only for the interesting discussions we had, but also for being a really good and fun friend. Everyone in the Kaon Cluster Group are really cool people, however I would like to thank in particular to Dr. Eliane Epple, Dr. Jia-Chii Berger-Chen and soon to be a Doctor Oliver Arnold for responding to all of my questions, regardless of their stupidity coefficient. Another guy that certainly made my life easier was soon to be a Doctor Rafal Lalik, who helped me to solve all computer-related issues that I had.

The other people responsible for me successfully bringing this chapter of my life to an end are, without a shadow of a doubt, my family. It goes without saying that they all were always supportive, but I would like to especially thank my parents and grandparents for being the perfect role-models and fueling my desire to never stop exploring the world surrounding us. But as it sadly often happens nowadays, almost every dreamer is being brought to ground when the bills arrive. Here I would like to give my mother Boriana a huge hug and a high-five for financially supporting me during all this years. Hopefully this will not be needed any more and she will finally be able to make her dream-journey to Machu Picchu :) And last, but definitely not least, I must give another high-five. This one goes to my girlfriend Iva who, despite me being a total nerd at times, somehow decided to stay around. And, even though she herself had some pretty rough moments, she always found the strength to be understanding and patient when I most needed it. Oh yeah, and I practiced all my talks in front of her, so she might be able to explain even better than me what I did for this thesis :)

Many words but one conclusion: thanks guys, you are all awesome!

Contents

Declaration of Authorship	i
Abstract	ii
Acknowledgements	iii
Contents	iv
Abbreviations	vi
List of Figures	vii
List of Tables	viii
1 Introduction	1
1.1 Notation	1
1.2 $K^*(892)^+$	2
1.2.1 General properties	2
1.2.2 Production mechanism	2
1.2.3 Detection mechanism	3
1.3 Motivation	4
1.3.1 Possible modifications of $K^*(892)^+$	4
1.3.2 Existing experimental data	7
1.4 Structure of this work	8
2 General concepts	10
2.1 Particle reconstruction in an experiment	10
2.2 Invariant mass	13
2.3 Acceptance and efficiency	14
3 The HADES experiment	18
3.1 Overview	18
3.2 Detector system	18
3.3 Access to the data	22
3.4 Simulation tools	23

4	Analysis of the $K^*(892)^+$ production	25
4.1	Experimental data	25
4.2	Simulated data	26
4.3	Extraction of the total production cross section	27
4.3.1	Overview of the analysis	27
4.3.2	Topological cuts	30
4.3.2.1	Track selection and particle candidates	30
4.3.2.2	Additional cuts	32
4.3.3	Description of the signal	34
4.3.3.1	Phase space effects	35
4.3.3.2	Detector resolution	36
4.3.3.3	Fitting function	38
4.3.4	Correction for acceptance and efficiency	42
4.3.4.1	The two-channel model	43
4.3.4.2	Branching ratios	46
4.3.4.3	Extraction of the cross section	49
4.3.5	First results	50
4.3.6	Investigation of the systematic error	51
4.3.7	Final results	52
4.4	Spin alignment effects	54
5	Summary and conclusions	58
A	Neutral kaons	60
B	Phase space effects on the spectral shape	62
C	Number of simulated events	66
D	Uncorrected spectra	68
E	Conditions regarding the quality assurance	69
F	Legendre polynomials	70
	Bibliography	71

Abbreviations

AE	A cceptance and E fficiency
AEC	A cceptance and E fficiency C orrection
BW	B reit W igner
CM	C enter of M ass
DST	D ata S ummary T ape
FAIR	F acility for A ntiproton and I on R esearch
GSI	G SI H elmholtz C entre for H eavy I on R esearch
HADES	H igh A cceptance D i- E lectron S pectrometer
HI	H eavy- I on
IM	I nvariant M ass
IMS	I nvariant M ass S pectrum
PID	P article I Dentification
PS	P hase S pace
PSF	P hase S pace F unction
PV	P rimary V ertex
QCD	Q uantum C hromo D ynamics
QGP	Q uark- G luon P asma
SIS	H eavy- I on S ynchrotron (S chwerionensynchrotron)
SV	S econdary V ertex
tRPCs	timing R esistive P late C hambers
WLOG	W ithout L oss O f G enerality

List of Figures

1.1	Decay scheme of K^{*+}	4
1.2	The QCD phase diagram	5
1.3	Stages of the space-time evolution of a heavy ion collision	6
1.4	Excitation functions for kaons	8
2.1	An example of a PID using the specific energy loss	12
3.1	Imploded view of HADES	19
3.2	Schematic layout of the HADES detector	19
3.3	Schematic layout of the RICH detector	20
4.1	Energy loss in the MDCs	28
4.2	Double counting during the K^{*+} reconstruction	32
4.3	IMS of K_S^0	33
4.4	IMS of K^{*+} without a cut on $\text{IM}(K_S^0)$	33
4.5	IMS of K_S^0	34
4.6	Influence of the phase space on the spectral shape	35
4.7	Influence of the phase space on the spectral shape at high p_T	35
4.8	The IMS of K^{*+} in a PLUTO simulation using higher beam energy	37
4.9	Phase space correction function (PSF)	37
4.10	$\text{IM}(K^{*+})$ assuming a zero width	38
4.11	Comparison between Breit-Wigner and Voigt functions	38
4.12	The work-flow of the fitting procedure	41
4.13	Extraction of σ from a HGeant simulation	41
4.14	Experimental IMS of K^{*+}	42
4.15	Uncorrected p_T spectrum of K^{*+}	46
4.16	Clebsch-Gordan coefficients	48
4.17	Corrected IMS - First results	50
4.18	Systematic error of the total K^{*+} production cross section	53
4.19	Systematic error of the Σ -channel contribution	54
4.20	Corrected spectra of K^{*+}	55
4.21	Corrected $\cos\vartheta_{K_S^0}$ IMS of K^{*+}	56
4.22	Calculation of the systematic uncertainty of ρ_{00}	57
5.1	Updated excitation functions for Kaons	59
D.1	All uncorrected spectra of K^{*+}	68

List of Tables

1.1	The most probable K^{*+} production channels	3
4.1	Variables used to apply topological cuts to isolate the K^{*+} decay	30
4.2	Initial selection criteria	32
4.3	List of the commonly used cuts in this work	42
4.4	Notation rules used for the AEC	44
4.5	Isospin properties	48
4.6	First results for the total K^{*+} production cross section	51
4.7	Rules for selecting the cut-combinations	52
4.8	Conditions for accepting the analysis result for a specific topological cut	52
4.9	Final results for the total K^{*+} production cross section	53

Chapter 1

Introduction

The introduction will firstly give an overview of the notation and the main properties regarding the particle that will be investigated in this work: $K^*(892)^+$. The performed analysis will be justified at the end of the chapter.

1.1 Notation

In this work the following conventions regarding the notation are used.

Units

Unless specifically stated otherwise, natural units are used, in which the speed of light c and the Planck constant \hbar are both set to 1.

$$c = \hbar = 1. \tag{1.1}$$

This choice of units is called “natural” since they simplify certain equations and beautifully highlight the equivalence between energy, mass and momentum, because all three of them are given in the same units. By convention the unit of energy is eV.

Vectors

Both four-vectors and standard three-dimensional (3D) vectors will be used in this work. In order to avoid any confusion in the text “normal” 3D vectors are designated with lowercase and marked by an arrow, e.g. \vec{p} , while their corresponding magnitudes are without arrows, e.g. p . The four-vectors are denoted with an uppercase, e.g. P .

Particles

The notation regarding the particle species used in this work is that commonly accepted by PDG [7]. A nucleon, i.e. a particle that is either a proton or a neutron, is denoted by the letter ' N '. It is customary to use the term hyperon (Y) for baryons containing at least one strange quark. In this work the baryons containing exactly one strange quark, i.e. the Λ and Σ particles, will be of particular interest. Thus the term hyperon will be explicitly used for those two families of particles. The letter ' Y ' will be used for the ground states of the Λ and Σ , ' Y^* ' will be used for the resonance states $\Lambda(1405)$ and $\Sigma(1385)$. Since $K^*(892)^+$ will be frequently referred to, it will be shortly denoted as K^{*+} .

1.2 $K^*(892)^+$

1.2.1 General properties

K^{*+} is a short-lived mesonic resonance. Similarly to the K^+ meson it consists of an up- and an antistrange quark ($u\bar{s}$) and has an isospin $I = 1/2$, $I_3 = 1/2$ and an odd parity. Unlike the K^+ meson, which is a pseudoscalar meson with spin 0, K^{*+} is a vector meson, meaning that it has a total spin of 1. It mainly decays into a kaon and a pion via the strong interaction. The probability of any other decay is less than 0.3 %. When produced in hadronic reactions it has a mass of $M = 891.66$ MeV and a decay width $\Gamma = 50.8$ MeV. Those facts are taken from the PDG summary table [8].

1.2.2 Production mechanism

This analysis uses data from proton-proton collisions with a center of mass energy of $\sqrt{s} = 3.18$ GeV. The observable \sqrt{s} is the invariant mass of the system. Therefore the mass of the products cannot exceed the value of 3.18 GeV. The excess energy of a reaction is defined as

$$\varepsilon := \sqrt{s} - \sqrt{s_{\text{thr}}}. \quad (1.2)$$

The threshold energy $\sqrt{s_{\text{thr}}}$ is the minimum amount of energy required for a certain final state and corresponds to the sum of the masses of all constituent particles. All three-body final states with a positive ε are listed in table 1.1. There are numerous

#	Reaction	$\sqrt{s_{\text{thr}}}$ [MeV]	ε [MeV]
1.	$p + p \rightarrow p + \Lambda + K^{*+}$	2946	231
2.	$p + p \rightarrow n + \Sigma^+ + K^{*+}$	3021	156
3.	$p + p \rightarrow p + \Sigma^0 + K^{*+}$	3023	154
4.	$p + p \rightarrow N + Y + \pi + K^{*+}$	≥ 3081	≤ 96
5.	$p + p \rightarrow N + Y^* + K^{*+}$	≥ 3214	≤ -37
6.	$p + p \rightarrow p + N + K + K^{*+}$	≥ 3262	≤ -87

TABLE 1.1: Some of the most probable K^{*+} production channels. The ones that are grayed out are considered to be significantly suppressed compared to the first three reactions.

other possible final states, but all of them are suppressed either because they have a negative excess energy and/or have more than three particles in the final state.

1.2.3 Detection mechanism

Due to its very short mean lifetime, K^{*+} decays very close to its production location long before it can reach the detector. Thus, the only way to reconstruct the particle is through the investigation of its decay products. As mentioned in section 1.2.1, the dominant decay mode of the K^* results in the state $K + \pi$. In the case of K^{*+} there are two possibilities:

$$K^{*+} \rightarrow K^0 + \pi^+, \quad (1.3)$$

and

$$K^{*+} \rightarrow K^+ + \pi^0. \quad (1.4)$$

The π^0 cannot be efficiently detected by HADES since the experimental set-up is not directly sensitive to neutral hadrons. An indirect detection of π^0 is also not possible, since it mainly decays into a pair of photons, which the HADES detector is not capable to detect. Thus it is impossible to detect the K^{*+} meson using the decay mode 1.4. The $\pi^{+/-}$ on the other hand are very easy to be directly detected, since the tracking system is very sensitive to them and they have a decay length, i.e. average distance before the particle decays, of ≈ 7.8 m, which allows them to reach the detector. The K^0 meson can be detected from its decay products using the invariant mass technique, which will be explained in the next chapter. Note that K^0 has two distinct weak eigenstates, i.e. states with definite lifetimes under decays via the weak force [9, 10], which are the K_S^0 and the K_L^0 (see appendix A for further discussion). K_S^0 has a decay length of ≈ 27 mm and predominantly decays to $\pi^+ + \pi^-$. Thus most of the K_S^0 particles decay before

they have reached the tracking system and their decay products are easily detected afterwards. Therefore K^{*+} can be reconstructed using the following decay scheme:

$$K^{*+} \rightarrow K_S^0 + \pi^+ \rightarrow \pi^+ + \pi^- + \pi^+. \quad (1.5)$$

The topology of the process is illustrated in figure 1.1, highlighting the fact that the K^{*+} decays almost instantly but, on average, the K_S^0 particles decay several tenths of millimeters away from the primary vertex. This feature, as it will be explained later, is of great importance for reconstructing the K^{*+} .

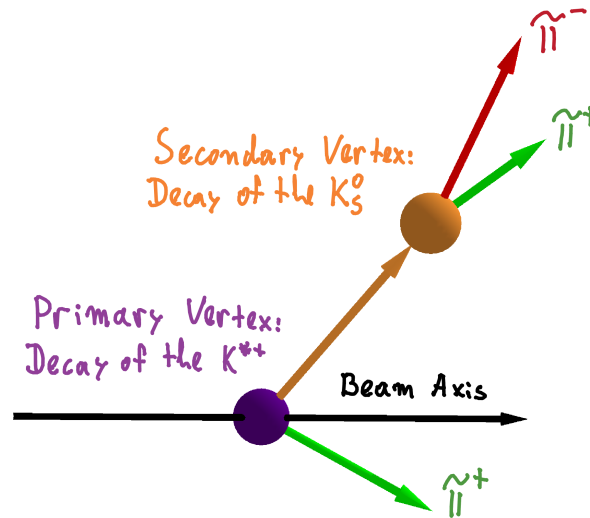


FIGURE 1.1: The K^{*+} decays almost instantly at the primary vertex (PV) into $K_S^0 + \pi^+$. The K_S^0 travels some distance before decaying into $\pi^+ + \pi^-$ at the secondary vertex (SV). This example is from a real event, the visualization was performed using GeoGebra [11].

1.3 Motivation

1.3.1 Possible modifications of $K^*(892)^+$

Within the Standard model of physics (see for example [10, 12]) the strong interaction is described by the quantum chromodynamics (QCD). Since QCD is asymptotically free, the interaction becomes weaker at higher energies [13]. Thus it is predicted that at extreme energy densities hadrons break up and the matter is transformed into a new phase called quark gluon plasma (QGP). In this state the chiral symmetry is presumably restored and the quarks are deconfined. There are still some disputes regarding the exact properties of the QCD phase diagram but it is commonly accepted that at

high temperatures or for a high chemical potential corresponding to a high net baryon density, a transition to QGP should occur. A sketch of the QCD phase diagram is shown in figure 1.2. Different collision experiments can probe different regions of this

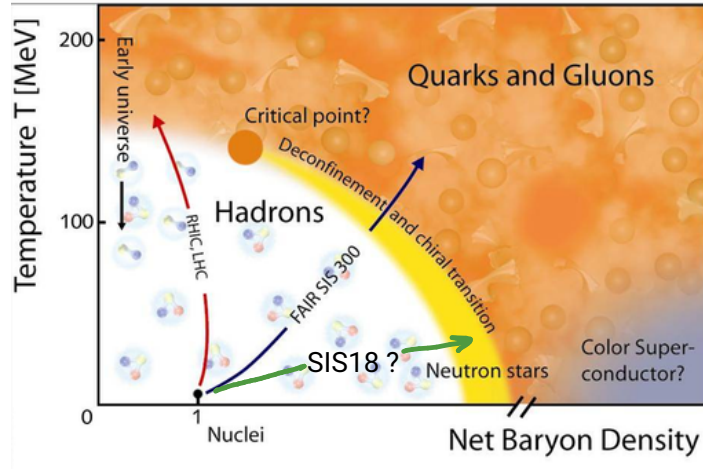


FIGURE 1.2: The QCD phase diagram [14].

diagram. In particular, at SIS18 the HADES experiment has access to relatively low temperatures and high chemical potentials. When a heavy-ion (HI) collision is realized in an experiment, the matter passes through several phases before reaching the detector. First a *fireball* is created, which is either in QGP phase or a hadron gas phase. As the system expands, its energy density decreases. If a QGP state was realized, it transitions back to a hadron gas state. In the next stage of the development of the system the hadrons scatter off each other both elastically and inelastically, i.e. the particle composition continues to change. At a certain threshold value the energy density of the system becomes low enough so that only elastic scattering can occur. This is known as the *chemical freeze-out* [15]. The system further grows in size so much that the mean free path of the particles is larger than the radius of the fireball. At this point all particles practically stop to interact and continue to fly towards the detector. This is called the *thermal (kinetic) freeze-out* [15]. These stages are schematically represented in figure 1.3. It is important to note that the yields of all particle species are fixed after the chemical freeze-out. This implies that most of the particles reconstructed by the detector are created before the occurrence of chemical freeze-out. Thus any effects of the medium are transferred to the kinematic observables of those particles. However, short-lived resonances that decay via the strong interaction, such as the $K^*(892)^+$, can

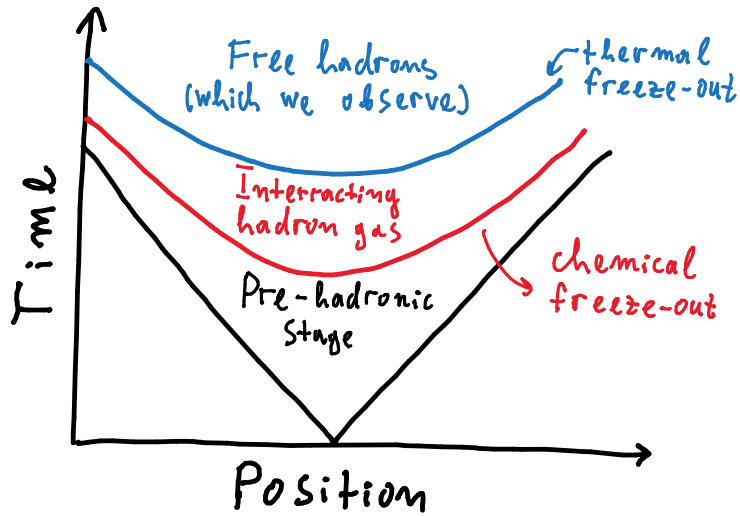


FIGURE 1.3: Stages of the space-time evolution of a heavy ion collision. The sketch is created after [15].

be much more sensitive to in-medium effects because of several reasons. In particular there are a few competing effects that can change the detected yield¹ of a resonance:

- **Regeneration**

This is the process of pseudo-elastic scattering of the decay products through the corresponding resonance state, e.g. $K\pi \rightarrow K^* \rightarrow K\pi$ [16]. Unlike the initial $K\pi$ pair, the invariant mass of the scattered particles corresponds to $\text{IM}(K^*)$ and thus the total detected K^* yield should increase.

- **Re-scattering**

If some of the decay products of the resonant particle scatter within the interacting hadron gas² it will lose the direct kinematic correlation to its mother particle and thus the invariant mass technique will not be able to reconstruct the original resonance [16]. As a result the measured yield of the investigated species should decrease.

- **Partial restoration of chiral symmetry**

It is theoretically possible to probe the partial restoration of chiral symmetry, near the phase transition point, by searching for mass or width modifications of the observed resonances [16, 17].

¹The yield corresponds to the number of particles. The particle reconstruction is performed using the invariant mass technique (see chapter 2.2 for further details), thus the reconstructed yield will change if the kinematic properties of the daughter particles are changed.

²That is during the stage between the chemical and the thermal freeze-out.

- **In-medium potential**

There are theoretical models that predict a repulsive in-medium potential affecting K^+ and an attractive one affecting $K^*(892)^+$ [18]. The effect of such a potential can be tested using transport models, for example by investigating the shape of the transverse momentum (p_T) spectrum and searching for deviations from the zero potential expectation. An example of such study is the analysis performed by the HADES collaboration regarding the in-medium modification effects acting on K^0 [3]. The result of this study is consistent with the theoretical prediction of a repulsive potential acting on K^0 .

The exact strength of each effect depends on the properties of the medium. The hadronic medium can be tested by modeling it with transport models and comparing the predicted yields with the experimental data. In particular one is interested in cold or hot nuclear matter effects that deviate from the 0-hypothesis, according to which HI collisions are a superposition of many nucleon-nucleon collisions. For this reason it is essential that HI collision data are analyzed using a reference that does not contain any in-medium effects. The proton-proton (pp) system has this property and therefore it is the perfect benchmark.

1.3.2 Existing experimental data

The properties of $K^*(892)^+$ have not been previously measured at energies close to the production threshold in p+p reactions. As can be seen in figure 1.4, this is in contrast to K^+ , which has been measured inclusively as well as exclusively down to excess energies ε of less than 1 MeV. The lowest measurement of the total production cross section of $K^*(892)^+$ in p+p reactions currently lies at $\sqrt{s} = 4.93$ GeV [19], which corresponds to an excess energy of $\varepsilon = 1.99$ GeV. The HADES experimental data for p+p collisions at $\sqrt{s} = 3.18$ GeV allows for probing $K^*(892)^+$ at an excess energy of only $\varepsilon = 0.23$ GeV.

In summary: The obvious lack of data for the production of the $K^*(892)^+$ resonance at near-threshold energies ($\sqrt{s_{\text{thr}}} = 2.95$ GeV) and the rich possibilities to test in-medium effects using this particular resonance inspired us to perform a study using the HADES data for pp collisions at $\sqrt{s} = 3.18$ GeV. This will fill the currently existing huge experimental gap and will provide valuable inputs for transport models. The result presented here can be used as a reference to p+A or A+A collisions at comparable

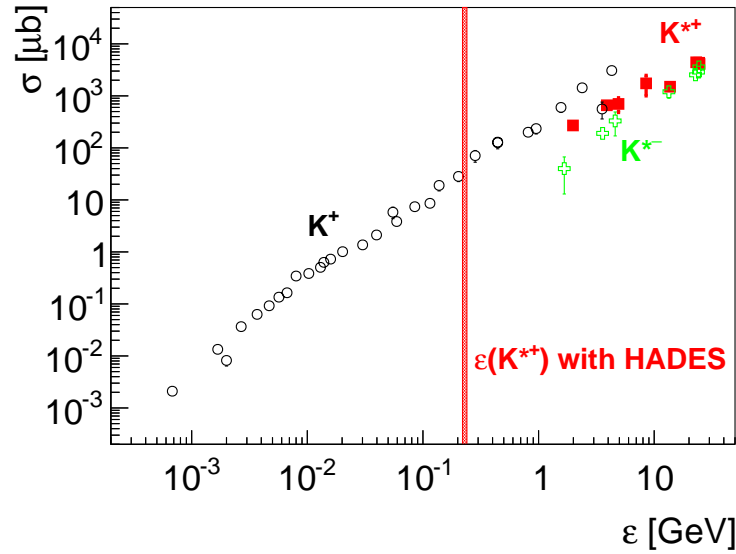


FIGURE 1.4: The cross section as function of the excess energy for: (i) $pp \rightarrow K^*(892)^+ X$ (red squares), (ii) $pp \rightarrow K^*(892)^- X$ (open green crosses), and (iii) $pp \rightarrow K^+ X$ (open circles) [6]. The red line marks shows the energy region accessible by HADES for $K^*(892)^+$.

energies, which can provide information about in-medium effects. Currently there are data collected by HADES at 3.5 GeV kinetic beam energy for p+Nb collisions. This particular types of collisions are expected to create cold nuclear matter, which probably does not transition into a QGP phase. Nevertheless even at saturation density partial restoration of the chiral symmetry is expected. Regeneration effects might not take place, since the pNb system is relatively small and dilute. In the future the newly constructed FAIR [20] facility will accommodate the HADES experiment and will provide higher beam energies using the synchrotron SYS100 [21]. It will then be possible to perform A+A collisions at those energies.

1.4 Structure of this work

This work contains an analysis of the $K^*(892)^+$ production in p+p collisions at $\sqrt{s} = 3.18$ GeV and it is structured as follows:

- **Chapter 2: General concepts**

The basics of particle detection and reconstruction as well as the invariant mass technique and the effect of acceptance and efficiency are explained.

- **Chapter 3: The HADES experiment**

This chapter gives an overview of the HADES experiment and its detector systems. The capabilities and limitations of the detector are shortly described. The chapter also introduces the main software tools that are provided by the HADES collaboration and used in this work.

- **Chapter 4: Analysis of the $K^*(892)^+$ production**

This is the main chapter of this study. It explains all steps of the data analysis, the extraction of the total production cross section of $K^*(892)^+$ and the investigation of spin-alignment effects.

- **Chapter 5: Summary and conclusions**

Chapter 2

General concepts

2.1 Particle reconstruction in an experiment

The reconstruction of particles from the detector response is a complicated procedure. Certainly the interaction of a single particle with the detector happens on a microscopic scale. The basic idea is to allow for the propagation of the microscopic interaction to macroscopic effects leading to a stronger signal, for example a current, significant enough to be measured. The signal then needs to be digitalized and the obtained raw signal can be further used for the reconstruction procedure. In this chapter a brief overview of the concepts most relevant to the performed analysis will be given.

Track reconstruction

A particle propagating through the detector produces *hits*. A hit is the measured location of the particle within the detector. The hits can then be used to reconstruct the *track* of the particle. A track is an object that contains information about the particle spatial and kinematic characteristics. The spatial trajectory of a particle can be directly obtained using the hits. For charged particles it is possible to use an external magnetic field in order to bend their trajectories. The bending radius can be used to extract the momentum of the particle. In addition, the direction of the bending provides information about the charge of the particle, i.e. whether it is negative or positive.

Particle identification

So far the track carries information about the position, momentum and charge of the particle. A very important and needed property is the mass. One way to obtain it is

to use the specific energy loss of a particle inside a certain medium. The term *stopping power* is used to describe the force acting on a charged particle propagating through a medium. The *linear stopping power* is:

$$S(E) = -\frac{dE}{dx}, \quad (2.1)$$

and describes the energy loss per unit length within the material. For practical reasons in many physics books the term *energy loss* is used to describe the *mass stopping power*, which is the linear stopping power divided by the density of the medium. The average energy loss of a particle is commonly written as

$$-\left\langle \frac{dE}{dx} \right\rangle.$$

This might be slightly misleading, since the units are not $\text{eV} \cdot \text{cm}^{-1}$ as in the case of $S(E)$, but rather $\text{MeV} \cdot \text{g}^{-1} \cdot \text{cm}^2$! In order to be consistent with the literature this notation is also used in the present study. A detailed discussion on the *passage of particles through matter* can be found in the Review of Particle Physics [7]. The equation of interest to us is the Bethe-Bloch formula:

$$-\left\langle \frac{dE}{dx} \right\rangle(\beta) = K \frac{Z}{A} \frac{z^2}{\beta^2} \left[\frac{1}{2} \ln \left(\frac{2m_e c^2 \beta^2 \gamma^2 T_{\max}(\beta)}{I^2} \right) - \beta^2 - \frac{\delta(\beta)}{2} \right], \quad (2.2)$$

which describes the mean rate of energy loss by moderately relativistic ($\beta\gamma \sim (0.1, 100)$) charged heavy particles. In the last equation:

$$K = 0.307075 \text{ MeV mol}^{-1} \text{ cm}^2,$$

m_e is the mass of the electron,

c is the speed of light,

Z is the atomic number of the absorber,

A is the atomic mass of absorber (in g mol^{-1}),

z is the charge number of incident particle,

β is the velocity of the particle (in natural units),

$\gamma = 1/\sqrt{1 - \beta^2}$ is the Lorentz factor,

I is the characteristic ionization constant of the gas,

δ is a density correction term.

T_{\max} is the maximum kinetic energy that can be transferred to an electron in a single collision. It is described by the equation:

$$T_{\max} = \frac{2m_e c^2 \beta^2 \gamma^2}{1 + 2\gamma m_e/m + (m_e/m)^2}, \quad (2.3)$$

where m is the mass of the incident particle. These equations are by default expressed as a function of β but, certainly, one could rewrite them as a function of the momentum $p = \beta\gamma m$. This is extremely useful since the HADES experiment measures the momenta of the particles and, as shown in fig. 2.1, $\langle \frac{dE}{dx} \rangle(p)$ has very distinct functional shape for different mass of the incident particle, which allows us to perform a particle identification (PID) based on this relation. Thus if both the momentum and the energy loss are measured, the mass of the particle can be determined!

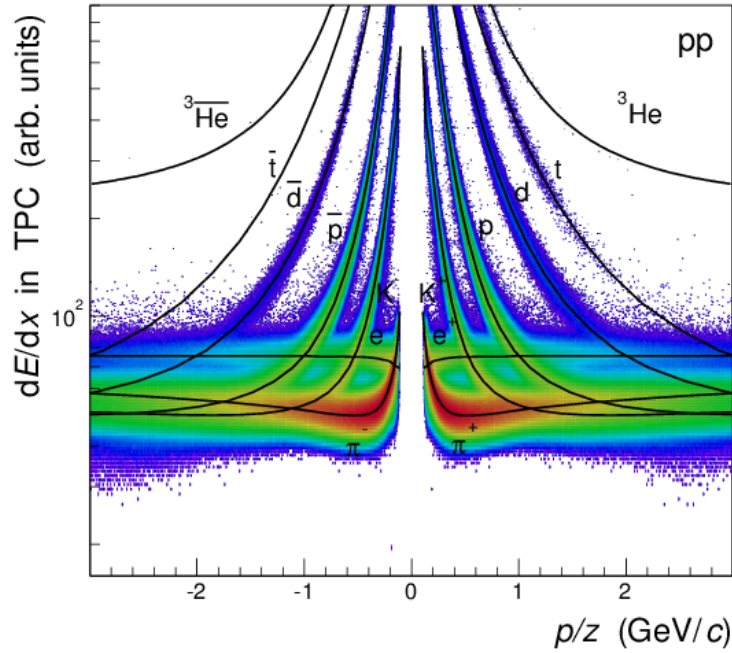


FIGURE 2.1: An example from the ALICE experiment [22] of a PID using the specific energy loss technique. The black curves represent the theoretical expectation, the colored areas represent the amount of experimentally detected hits. The color scale is based on the yield: red - many hits; blue - only a few hits. On this particular plot the momentum is divided by the charge number (z) of the particle. The calculation for the electron is performed differently since they are significantly lighter and thus experience radiative energy losses.

In a real experiment there are always uncertainties in all of the measured quantities. Therefore the detected particles will be distributed around the theoretical lines rather than lying exactly at the expected position. This results in a slight overlap of the distributions, especially at high momenta. Thus the different particle species will become

indistinguishable from each other. Therefore in a real-life experiment some of the particles are misidentified. The number of misidentifications can be lowered at the expense of the statistics by applying stricter cuts around the theoretical curves. Normally it is impossible to achieve perfect particle identification, thus there is always a certain probability that a track has a false PID assigned to it. For this reason the term *particle candidate* will be used whenever referring to a reconstructed particle, highlighting the possibility of misidentification.

There are other methods to perform a PID. One that can generally be applied to the HADES data is the use of *time of flight* information, although for reasons that will be clarified in the following chapters it cannot be used in this analysis. The time of flight is defined as the time it takes for a particle produced in an event to reach a time-measuring detector. This requires to know not only the time of arrival of the particle, but the zero-time of the event as well. Since the distance to the detector is known, one can calculate the velocity β of the particle. The momentum of the particle is usually a measurable quantity, thus one can obtain the mass using the equation:

$$p = \beta\gamma m = \frac{\beta}{\sqrt{1 - \beta^2}} m, \quad (2.4)$$

$$\Rightarrow m = \frac{p\sqrt{1 - \beta^2}}{\beta}. \quad (2.5)$$

2.2 Invariant mass

Particle detectors can directly detect only certain types of particles. There are two general reasons for this. First, different particles interact with matter differently, thus the design of an experimental system should always make a compromise regarding which particle species can be measured directly. Second some particles are short-lived and decay before they have reached the detectors. I will now discuss the latter case and introduce the concept of the invariant mass (IM). The basic idea is to reconstruct a particle from its decay products that are assumed to be directly measurable, by using the fundamental law of energy and momentum conservation. In the following I will use the notation of four vectors (see for example [10]) and the energy-momentum relation 2.6.

$$E^2 = m^2 + p^2. \quad (2.6)$$

The corresponding four-momentum vector is defined as:

$$P = \begin{pmatrix} E \\ \vec{p} \end{pmatrix}. \quad (2.7)$$

Let us assume that N_i initial number of particles interact with each other and they end up in N_f number of particles. The conservation of energy and momentum is given by the equation:

$$\sum_{k=1}^{N_i} P_{i,k} = \sum_{k=1}^{N_f} P_{f,k}, \quad (2.8)$$

where P_i and P_f are the four-momenta of the initial and final particles respectively. The multiplication of two four-momenta is by definition given as:

$$P_1 \cdot P_2 = E_1 \cdot E_2 - \vec{p}_1 \cdot \vec{p}_2. \quad (2.9)$$

This means that:

$$\boxed{P^2 = E^2 - p^2 = m^2 =: s}. \quad (2.10)$$

This observable is always invariant under Lorentz transformations. Lets now investigate the the decay of a mother particle into N daughter particles. From eq. 2.8 it follows that:

$$P = \sum_{k=1}^N P_k, \quad (2.11)$$

where P is the four-momentum of the mother particle and P_k are the momenta of the daughter particles. This means that as long as one knows the energies and momenta, or equivalently the mass and momenta (eq. 2.6), the four-momentum of the mother particle is well defined (see 2.7). The mass of the particle can now be calculated using equation 2.10.

2.3 Acceptance and efficiency

Overview

Each detector has some limitations regarding its sensitivity. The types and properties of the particles that a detector can measure defines the acceptance. Even if a detector is sensitive to a particular type of particles, lets say pions (π), no detector will ever be able to record each and every pion, but will only be sensitive to a particular sub-set

of the available phase space¹, for example pions with very low or high momenta might not be detected at all. Furthermore even if a particular π can be detected, depending on its position in the phase space the detector is able to record it only with a certain probability. This probability is called the efficiency of the detector. It is important to emphasize that the efficiency of the detector is not a constant but rather a variable that depends on the position in the phase space. If one is interested in the yield² of a certain particle species, one should always take into account the fact that the detector efficiency reduces the detected yield. In the extreme case of zero efficiency, i.e. outside of the acceptance, there is a zero yield in the experiment. Thus it is of great importance that the acceptance and efficiency of the detector system are well understood. If this is the case, one can easily correct the obtained experimental yield and calculate the actual yield. Let us consider a specific example in which it is assumed that the position in the phase space is fully defined by the momentum-vector of the particle. Let N be the total yield (number of particles) and ΔN be the yield in a very small volume of the phase space. Then the following relations are valid:

$$\Delta N = C(p, \theta, \varphi) \times (\Delta N)_{\text{det}}, \quad (2.12)$$

$$\Delta N = \frac{\partial^3 N}{\partial p \partial \theta \partial \varphi}, \quad (2.13)$$

$$(\Delta N)_{\text{det}} = \left(\frac{\partial^3 N}{\partial p \partial \theta \partial \varphi} \right)_{\text{det}}, \quad (2.14)$$

where the subscript “det” denotes the detected yield and C is a correction function that relates the real and detected yields. Many of the particle detector systems, including HADES, are symmetrical with respect to φ , thus we can consider C as a function of p and θ only, i.e.

$$\Delta N = C(p, \theta) \times (\Delta N)_{\text{det}}, \quad (2.15)$$

$$C(p, \theta) = \frac{\Delta N}{(\Delta N)_{\text{det}}}. \quad (2.16)$$

Once obtained, this function can be used to correct the experimental data for the effects of the acceptance and efficiency.

¹A space (in a mathematical sense) containing all possible states of a dynamical system.

²Number of particles produced in the investigated reaction.

Differential analysis

By differential analysis we understand the treatment of $C(p, \theta)$ as a discrete function, which so far has been defined as a continuous function. Hence $C(p, \theta)$ can be represented by a matrix called by convention acceptance and efficiency correction matrix (AEM). The most common way of obtaining the AEM is by means of simulations. This can be achieved by a two-step method. Firstly one can use a Monte-Carlo (random) event generator to simulate particles with different phase space parameters. Secondly one needs to reproduce the propagation of the previously simulated particles through the detector system and the response of the system. This is a very complicated procedure and commonly performed using the Geant platform. Geant is “a toolkit for the simulation of the passage of particles through matter” [23]. By discretizing the phase-space and making sure that we have enough number of simulated events in each phase-space-bin, one can calculate the AEM by dividing bin-wise the number of particles originally simulated with the Monte-Carlo event generator by the number of particles recorded after running Geant. Thus the coefficients C_{ij} of the AEM can be calculated using the following equation:

$$C_{ij} = \frac{\Delta N_{ij}}{(\Delta N)_{\text{det},ij}} \approx \frac{(\Delta N)_{\text{MC},ij}}{(\Delta N)_{\text{Geant},ij}}. \quad (2.17)$$

In a simulation all parameters and output values are known. Hence $(\Delta N)_{\text{MC},ij}$ and $(\Delta N)_{\text{Geant},ij}$ can be used to compute C_{ij} . Obviously the detected yield $(\Delta N)_{\text{det},ij}$ is a known parameter during an experiment, hence the quantity of interest ΔN_{ij} can be obtained using:

$$\Delta N_{ij} = C_{ij}(\Delta N)_{\text{det},ij} = \frac{(\Delta N)_{\text{MC},ij}}{(\Delta N)_{\text{Geant},ij}}(\Delta N)_{\text{det},ij}. \quad (2.18)$$

Possible problems

This procedure has two main assumptions:

- The simulation of the detector is accurate.
- The discretization is fine enough, i.e. the number of bins is very big.
- The geometric acceptance of the detector is limited.

The first condition is taken for granted since Geant is a pretty advanced platform that is proven to be very robust. The second part is mostly limited by the statistics. Generally speaking the initial simulation does not need to be physically accurate in order to apply

the AE correction. The reason is that we only look at an infinitesimally small region of phase-space and thus can assume a uniform distribution of the particle production within this region. In contrast, if the discretization is coarser there might be some physical effects that make the production non-uniform over a certain domain in phase-space. Therefore the simulated production yield, and consequently the whole correction procedure, will be inaccurate. More precisely: a fine discretization is independent of the model used to populate the phase-space and a coarse discretization is model-dependent. For this reason it is of great importance to refine the binning as much as possible. Alternately one should have a much deeper understanding of the production mechanism already at hand. Additionally any limitations in the geometric acceptance of the detector can lead to a zero yield in certain bins, i.e. $(\Delta N)_{\text{Geant},ij} = 0$. Unfortunately this issue cannot be resolved model-independently since the only two ways to overcome it is either by extrapolation or by coarser binning.

Chapter 3

The HADES experiment

3.1 Overview

The **H**igh **A**cceptance **D**i-**E**lectron **S**pectrometer (HADES) is a fixed-target experiment located at the GSI Helmholtz Centre for Heavy Ion Research in Darmstadt, Germany [24]. It is currently installed at the SIS18 accelerator which can provide a beam with kinetic energies of 1-2 GeV per nucleon. The detector was initially designed for measurements of the in-medium modifications of the ρ , ω and ϕ mesons via detection of their decay into a dilepton pair (e^+e^-). However the current physics program of HADES is far richer due to the capability of the detector system to reconstruct charged hadrons as well. This allows for investigation of multiple topics. One in particular, which is of interest in this work, is the strangeness physics, i.e. the production of particles containing a strange quark. For example in the recent past a detailed analysis of the neutral kaon production was performed by members of the HADES collaboration [3]. The present study benefits from those previous works since a lot of the developed framework, regarding kaon reconstruction, can be reused in this analysis.

A detailed description of the HADES set up can be found in [24]. In this chapter I will summarize some of the most important information regarding the experiment.

3.2 Detector system

The HADES detector system is composed of six identical sectors that are located around the beam axis (see figures 3.1 and 3.2). This allows for almost full azimuthal

coverage. The coverage in the polar angle is also large, ranging from 15° to 85° .

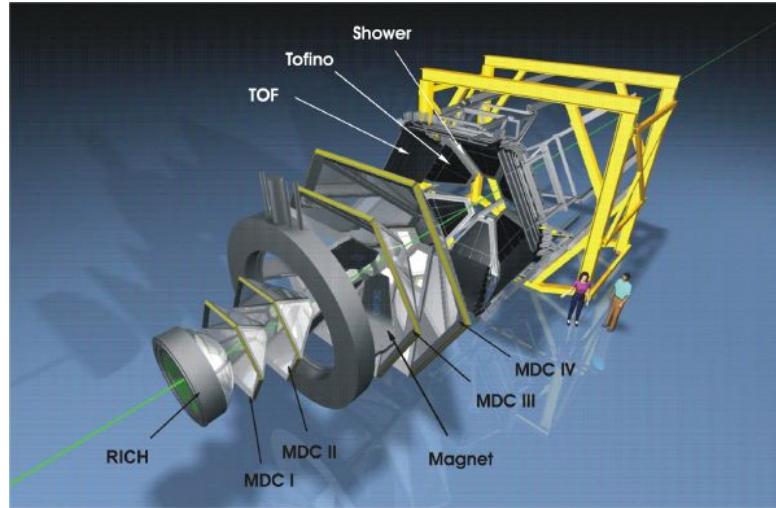


FIGURE 3.1: Imploded view of HADES [25].

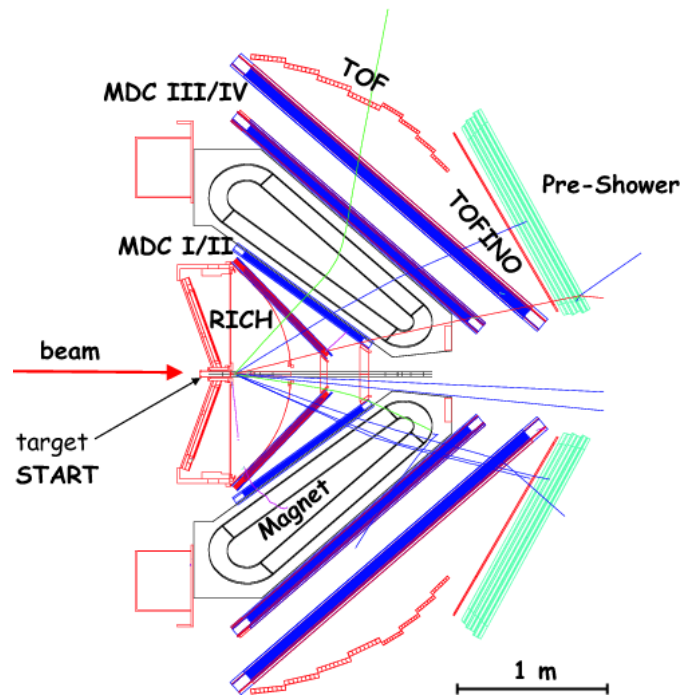


FIGURE 3.2: Schematic layout of the HADES detector - a side view [24].

The target

The target that the beam shoots at sits in-between the six sectors of HADES. It is located in a field-free region. There are different types of targets that can be installed. For proton-proton collisions a liquid hydrogen target was used.

The RICH detector

The **R**ing-**I**maging **C**herenkov (RICH) detector is used for the detection of relativistic electrons and positrons with momenta of $0.1 \text{ GeV} \leq p \leq 1.5 \text{ GeV}$. It covers the whole HADES acceptance. It essentially consists of two gas-volumes (see fig. 3.3), one is the radiator volume, which is filled with C_4F_{10} gas that has a threshold Lorentz factor for Cherenkov radiation of $\gamma_{th} = 18$. This means that only highly relativistic particles can be detected. From the general relation

$$\gamma = \frac{E}{m} \propto \frac{E_{kin}}{m} \quad (3.1)$$

it becomes clear, that in order to have high-enough γ one either needs a light particle or high kinetic energy. However in the momentum range of interest it is impossible for any hadron or muon to have high enough energy to produce Cherenkov radiation. Therefore the RICH detector is sensitive only to electrons and positrons. If an electron or a positron produces Cherenkov radiation the photons are reflected from a Vacuum-Ultraviolet (VUV) mirror. The photons then enter the photon detection volume, which is filled with methane and separated from the radiator volume by a CaF_2 window, and are focused on a photon detector in a ring-shaped pattern.

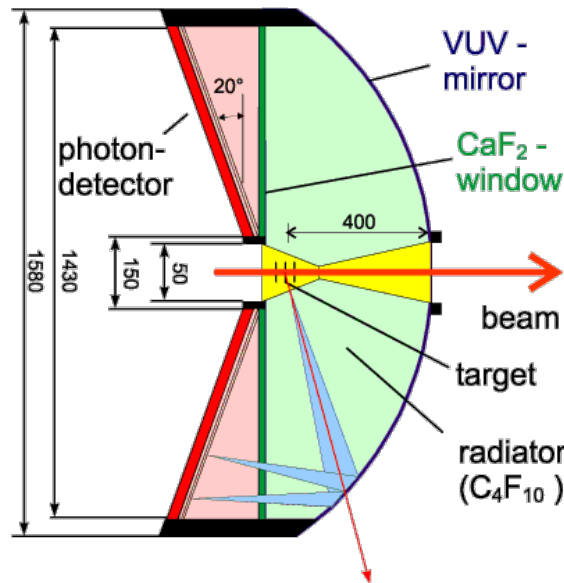


FIGURE 3.3: Schematic layout of the RICH detector [24].

The multi-wire drift chambers and the magnet

The **M**ulti-**w**ire **D**rift **C**hambers (MDCs) are located after the RICH detector and are

arranged in four planes. Each plane consists of six identical trapezoidal-shaped MDCs. Two of the planes are located before and two after a magnet. The MDCs are capable of measuring the position of the incoming particles. This is achieved by letting the particles propagate through a gas-filled drift chamber which leads to ionization of the gas. Each chamber is equipped with six wire-layers that are all arranged in different stereo angles to each other in order to improve the resolution. After the primary ionization the free electrons start drifting, due to an electric field, inducing secondary ionization and multiplication of the drift-electrons. Finally the electrons reach the wire-layers and a signal is created.

The magnet located between MDC planes I/II and III/IV creates a magnetic field, which causes the charged particles to bend according to their momentum. After that, based on the MDC position-hits and the known geometry of the magnetic field, the tracks of the particles are reconstructed, i.e. both the particle position and momentum. The spatial resolution of the system is in the order of $100 \mu m$ and the momentum resolution can be as good as 4%. The MDCs are suited for detection of charged particles only.

An additional feature of the MDC system is its capability to measure the energy loss of a particle. This is possible due to the fact that the deposited charge on the wires is proportional to the energy loss of the traversing particle. As explained in chapter 2.1, the energy-loss measurement is essential for the particle identification.

The META system

The **Multiplicity and Electron Trigger Array (META)** system consists of two time-of-flight detectors, TOF and TOFino, and an electromagnetic shower detector (Pre-Shower). TOF and TOFino are scintillator detectors that can measure the time of arrival of the particle with resolutions of 150 and 420 ps respectively. Both detectors can provide energy-loss information. In addition, the TOF detector is position-sensitive, although the spatial resolution is quite low (25-27 mm).

The Pre-Shower detector is located behind TOFino. It complements the TOFino detector by allowing for hit-position reconstruction as well as the RICH detector by its capability of lepton-hadron separation.

In 2009 several major upgrades were performed on HADES, one of which was the replacement of TOFino with a Resistive Plate Chambers (RPCs) detector. It features higher granularity and an improved time-resolution of ≈ 66 ps

The START-VETO system

In order to improve the particle identification capability of the Time-Of-Flight system a START-VETO system is used. A CVD (Chemical Vapour Deposition) diamond material was used to construct the START detector. It is located just in front of the target and is able to determine the reaction time. The VETO detector is located after the RICH detector and is made out of polycrystalline material. As the name suggests, it is used to veto all particles that have not interacted with the target but have been registered by the START detector.

The forward wall

In 2007 a deuterium beam experiment was performed [26]. It required the detection of forward proton spectators. Thus the forward wall was installed to cover the polar angle range from 0.33° to 7.17° . The forward wall is a scintillation hodoscope divided into 300 scintillating cells. It is capable of hit-position and time-of-flight measurements, as well as of energy-loss determination. However the momentum cannot be determined, which prohibits the particle identification.

The trigger system

The trigger system of HADES, which basically determines which events are recorded and which disregarded, consists of two levels:

- The **LVL1** trigger ensures that there is a certain minimum multiplicity (number of hits) in the META system.
- The **LVL2** trigger is optimized for the search of dilepton pairs. It uses the information from the RICH, TOF and Pre-Shower detectors for the signature of an electron or a positron.

Since storing only LVL2 events will significantly bias the hadron analysis, a down-scaled portion of the LVL1 events is saved as well. The downscaling is needed because of hardware and storage limitations. Such events are used in the presented analysis.

3.3 Access to the data

All data obtained from HADES is stored in specially formatted ROOT [27] files called Data Summary Tapes (DSTs). They contain detailed information about each event,

including full information about the reconstructed tracks. These files are accessible to all collaborators for further processing.

3.4 Simulation tools

As explained in chapter 2.3, it is necessary to be able to simulate the production and propagation of the analyzed particle in order to correct for AE effects. The HADES collaboration has developed and provided to all members a few very important tools that are suitable for this task.

PLUTO

The PLUTO framework is a Monte-Carlo event generator that is specifically developed for HADES [28]. It is suitable for simulating the production of particles in heavy-ion collisions at intermediate energies according to a thermal energy spectrum. In addition, it can be used to model the production of particles in elementary collisions, for example p+p. This is achieved under the assumption of a uniform phase space distribution. PLUTO allows for the implementation of a more specific angular distribution as well as for broader resonances. The latter is important for the simulation of the K^{*+} production. Additional feature of this software is the possibility to model the decay of a particle. This simulation tool is fully independent of the geometry of the experiment. The simulated yield corresponds to the coefficient $(\Delta N)_{MC,ij}$ in equation 2.17.

HGeant

The HGeant [29] simulation package is based on Geant 3.21 [23]. It includes implementation of the HADES geometry and is further modified in order to meet all requirements of the software framework used by the collaboration. It can use the tracks provided by PLUTO as an input and then simulates the propagation of the particles through the detector system. This includes all known effects, such as the deflection in the magnetic fields, scattering processes, energy loss, etc.

SimDST

The HGeant simulation itself does not provide an output that is equivalent to the DST format used for storing experimental data (see section 3.3). The SimDST simulation transforms the hits from the detector, which are provided by HGeant, into a realistic

signal. This includes all effects from the electronic readout of the experiment as well as track reconstruction. After this step the simulated data can be treated as experimental data, thus the yield of the investigated particle species obtained from the subsequent analysis corresponds to the $(\Delta N)_{\text{Geant},ij}$ coefficient in equation 2.17. As explained in section 2.3, this along with $(\Delta N)_{\text{MC},ij}$ available from PLUTO is enough to correct the experimental data for acceptance and efficiency.

Chapter 4

Analysis of the $K^*(892)^+$ production

4.1 Experimental data

The p+p 3.5 GeV beam

In the presented work p+p data at kinetic beam energy of 3.5 GeV were analyzed. The data were collected with the HADES spectrometer at GSI in April 2007. At that time the experimental setup was still using the TOFINO detector. The target was liquid hydrogen cooled down to 20 K at atmospheric pressure. The interaction probability was 0.7%. The beam time lasted three weeks during which 1.2×10^9 LVL1 events were recorded [6].

LVL1 trigger conditions

In the case of 3.5 GeV p+p collisions the LVL1 minimum multiplicity was set to three, which demands at least three particle candidates in the META detector (see chapter 3.2). This condition greatly suppresses the elastic p+p reactions in the data, which are needed only for normalization purposes. The elastic reactions are separately analyzed by the HADES collaboration, using a multiplicity requirement of two [30].

Detectors and data

The START detector was not used during this experiment due to the low energy deposition of protons in the diamond detectors [31]. This makes the determination of the

time-of-flight much more complex and inefficient. Thus this analysis makes use only of the data from the MDCs to detect the pions needed for the reconstruction of K^{*+} .

4.2 Simulated data

Simulating tools

The simulated data used in this analysis were obtained via the PLUTO and HGeant tools, as described in chapter 3.4.

Simulated channels

The AE corrections can be applied with a model-independent simulation of the phase space as long as the discretization of the correction function is very fine (see chapter 2.3) and the detector has a full geometric acceptance. Despite the big acceptance of HADES the latter condition is not fulfilled. In addition, as it will become evident later in this chapter, the statistics available for this analysis allows only for a very coarse discretization. Thus it is important to simulate the phase space distribution of K^{*+} taking into account the dominant physic effects. Since this is the first ever measurement of this particle species at this energy and HADES does not cover the full geometric acceptance, there is no available information about the angular distribution of K^{*+} and hence, one has to assume isotropic production. However, the possible production channels are known and therefore their kinematic properties can be taken into account during the simulations.

- $\mathbf{p + p \rightarrow N + Y + K^{*+}}$

Table 1.1 shows all reactions that have a three-body final-state and a positive excess energy ε . The dominating channel is expected to be the $p + p \rightarrow p + \Lambda + K^{*+}$ because it is energetically the most favorable one. Since the masses of the proton and the Σ^0 are very close to the corresponding masses of the neutron and the Σ^+ reactions 2 and 3 from table 1.1 are kinematically almost identical. Thus those two channels can be generalized by the reaction $p + p \rightarrow N + \Sigma + K^{*+}$ and it is sufficient to perform a PLUTO simulation on only one of the two Σ -related production channels. Without loss of generality (WLOG) the simulation was performed using the $p + \Sigma^0 + K^{*+}$ final-state.

- **$p + p \rightarrow N + Y + \pi + K^{*+}$**

The four-body final-state channels governed by this reaction are suppressed compared to the $p + p \rightarrow N + Y + K^{*+}$ channels due to the fact that the final state has one more particle and thus requires more energy (see the grey entries in table 1.1). The excess energy is still positive though, hence those channels definitely contribute to the total yield. However in a first order approximation they may be neglected. This assumption is an educated guess and it needs to be further verified. This issue will be addressed and discussed in section 4.3.4.1.

- **Off-shell channels**

The off-shell production of K^{*+} is possible due to the relatively large width of this resonance state ($\Gamma = 50.8$ MeV). Thus reactions 5 and 6 from table 1.1 can theoretically occur at energies lower than the threshold energy. Their contributions can be completely ignored since they are negligible compared to the sub-threshold channels.

In summary, only the final-states $p + \Lambda + K^{*+}$ and $p + \Sigma^0 + K^{*+}$ should be simulated. Further in this work this will be referred to as the *two-channel model*. The two channels will be referred to as the Λ - and Σ -production channel respectively.

Decay mode

Since the K^{*+} particle species is not included by default in the database of PLUTO, it was manually programmed into it. The mass and width of K^{*+} were set to their corresponding PDG values of $M = 891.66$ MeV and $\Gamma = 50.8$ MeV. The only implemented decay channel was $K^{*+} \rightarrow K_S^0 + \pi^+$. No other channels were needed since the reconstruction was performed using the K_S^0 decay channel exclusively.

4.3 Extraction of the total production cross section

4.3.1 Overview of the analysis

The extraction of the total production cross section of K^{*+} can be divided into several steps, all of which will be explained in detail in this chapter. A brief overview of those steps is given below:

Pion candidates

Using the DSTs provided by the HADES collaboration, the very first step is to assign to each track a PID by applying cuts on the energy loss vs momentum plot (fig. 4.1). As K^{*+} has to be reconstructed from the invariant mass of three pions (discussed in chapter 1.2.3), one needs to iterate over all particle tracks and select all pion candidates. The details about the pion identification procedure are given in the doctoral thesis of Dr. Jia-Chii Berger-Chen [31], as well as in [3, 32].

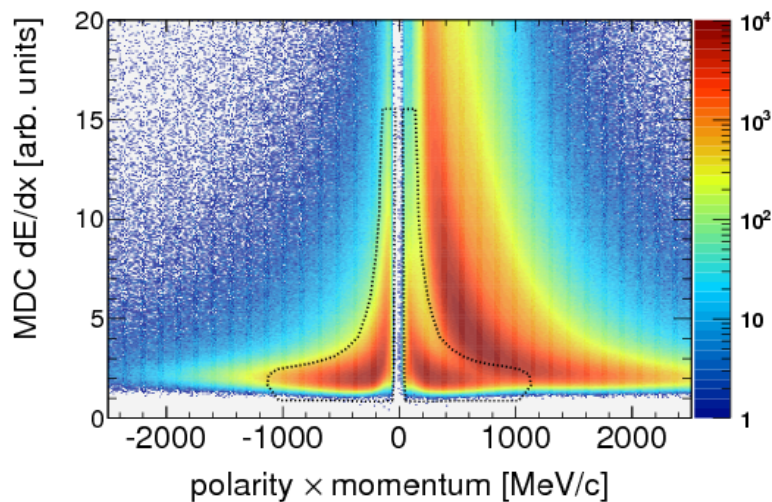


FIGURE 4.1: Energy loss dE/dx in the MDCs as a function of the momentum times the polarity of the track. The area enclosed by the dotted lines marks the events that are considered to be pions. For more details see [3] and [31].

K^{*+} candidates

The next step of the analysis is to combine the pions from each event in triplets, using one negative and two positive pions, in order to reconstruct the K_S^0 and K^{*+} candidates according to decay scheme shown in fig. 1.1. Each candidate needs to fulfill certain criteria in order to be selected for further processing.

Reduction of the S/B ratio

The selection criteria used so far are relatively loose. The next step of the analysis begins by plotting the invariant mass spectrum (IMS) of the K^{*+} candidates and fine-tuning the topological cuts until a good signal-to-background (S/B) ratio is achieved. This is necessary in order to have an apparent peak in the spectrum and be able to perform

a reliable fit. The K^{*+} yield can be subsequently extracted from the area of the fitted peak.

Choice of a fitting function

Fitting the IMS requires to know the spectral shapes of both the background and the signal. The background is commonly described by a simple polynomial function since the technique of event mixing does not work properly for p+p collisions. However the shape of the signal needs more attention. Resonance particles, including K^{*+} , can usually be described by a Breit-Wigner distribution, also known as Lorentz or Cauchy distribution. However, there are additional effects, most notably the detector resolution and phase space limitations, that can influence the spectral shape. Thus deeper investigation of those effects is needed when choosing the peak-shape fitting function.

Differential analysis and AE corrections

As explained in chapter 2.3 it is necessary to extract the yield in different kinematic bins in order to apply AE corrections independent of any model. Thus the data need to be divided into as many subsamples as possible and extract the yield for each bin. After that, the data can be corrected using the results obtained from the simulations.

From yield to cross section

The absolute yield has no physics meaning. The observable that has to be obtained is the cross section. It can be calculated by normalizing the K^{*+} yield to the yield of a process with a known cross section and measured during the same experiment. This can be achieved using the reference p+p elastic scattering that has been measured and documented by the HADES collaboration [30]. The obtained K^{*+} yield is only associated with its decay to $K_S^0 + \pi^+$ and thus the obtained cross section will correspond exclusively to this decay channel. In order to compute the total cross section, the branching ratios¹ of both the K^{*+} and the K_S^0 particles have to be taken into account. Those ratios can be very easily calculated using the Clebsch-Gordan coefficients [10].

Systematic error

The final step of the analysis is to investigate the systematic error by testing the analysis procedure for stability and reproducibility.

¹The branching ratio is the probability to decay via a certain channel.

4.3.2 Topological cuts

4.3.2.1 Track selection and particle candidates

After the tracks from the DST files obtain a PID, an iteration over all events is performed. Events that do not contain at least one π^- candidate and two π^+ candidates are disregarded. This condition is required by the decay scheme of the K^{*+} , shown in figures 1.1 and 4.2. The *primary vertex* (PV) and the *secondary vertex* (SV) are defined as the decay positions of the K^{*+} and the K_S^0 respectively. After selecting the triplets of pions the next step is to reconstruct the tracks of the K_S^0 and K^{*+} particles. This is achieved by combining two opposite charged pion candidates into a single K_S^0 candidate (at the SV) and then combining it with the remaining positive pion in order to reconstruct the K^{*+} candidate (at the PV). For each candidate a set of observables, that are important for the further processing of the data, are calculated and saved. They are listed in table 4.1.

Observable	Definition	Default cut
z_{PV}	The z position component of the PV.	$\in (-70; -10)$ mm
$d_{xy,PV}$	Distance from the PV to the beam (z) axis.	< 8.5 mm
$IM(K_S^0)$	Invariant mass of the K_S^0 candidate.	n/a
$IM(K^{*+})$	Invariant mass of the K^{*+} candidate.	n/a
d_V	Distance between the primary and the secondary vertex.	> 18 mm
$\delta_{\pi^+\pi^-}$	Distance of closest approach of the pions originating from the the K_S^0 candidate.	< 13 mm
$d_{\pi^{+/-}}^{K^0}$	Closest distance between the track of $\pi^{+/-}$ originating from the K_S^0 candidate to the primary vertex.	> 4 mm
$d_{\pi^+}^{K^*}$	Closest distance between the track of π^+ originating from the K^{*+} candidate to the primary vertex.	< 18 mm

TABLE 4.1: Variables used to apply topological cuts to isolate the K^{*+} decay. Note that $\delta_{\pi^+\pi^-}$ is ideally zero (the tracks intersect) but due to resolution effects this is never true.

After the particle candidates are reconstructed, further selection rules need to be applied in order to filter out as many fake candidates as possible. The basic idea is to constrain the candidates according to the topology of the reaction (fig. 1.1 and 4.2). It is important to keep the kinematic observables unconstrained, otherwise there is a risk to bias the data. The first filter (restrictions on z_{PV} and $d_{xy,PV}$) checks if the primary vertex, i.e. the K^{*+} candidate, is located within a cylinder around the target, oriented

in the direction of the beam. The length of the cylinder is 60 cm and its radius is 8.5 cm. This is a bit more than the size of the target, which is 25 cm in length and 5 cm in radius, but due to the resolution of the reconstruction procedure a real K^{*+} can be reconstructed slightly outside of the target. The next set of cuts are related to the relative position of the π and K_S^0 tracks to the two vertexes. The reason for constraining those observables is to make sure that the primary and secondary vertex are well separated and that the selected pion tracks are close to the vertex they have been assigned to. The exact values of the cuts are listed in table 4.1.

If there are more than three pion candidates in a single event, all possible combinations of $\pi^+\pi^-\pi^+$ are built and iterated over. This is necessary since there is no reliable way of recognizing which π candidates originates from a K^{*+} particle. This means that sometimes a single π candidate might be used for the reconstruction of more than one K^{*+} . However this is not a physical effect and possible “fake” K^{*+} candidates would simply populate the background in the invariant mass spectrum and would not interfere with the rest of the analysis. The term used to describe this effect is *combinatorial background*. After selecting the triplets of pions, the next step is to reconstruct the tracks of the K_S^0 and K^{*+} particles. This is achieved by combining two opposite charged pion candidates into a single K_S^0 candidate and then combining the K_S^0 track with the remaining positive pion in order to reconstruct the K^{*+} candidate. When reconstructing a particle using the IM technique the tracks of the daughter particles should ideally intersect, but due to the resolution effects of the detector and the tracking algorithm this is not the case. In the actual data those tracks have a small *distance of closest approach* but never intersect. Thus the point of intersection between the two daughter tracks, called a *vertex*, has to be extrapolated and usually lies along the line of closest approach of the two daughter particles. Since the initial selection is composed of two positive pions, there are two possible ways of combining them into a K_S^0 . It is possible that the alignment between the pion tracks is such that both combinations produce a reasonable secondary vertex, i.e. a K_S^0 candidate. Thus a triplet of pions may be *double counted* and used to reconstruct two K^{*+} candidates. An example, taken from a recorded event, is shown in figure 4.2. Similarly to the combinatorial background the double-counting effect will simply increase the background and will not interfere with the analysis. The strength of the two combinatorial effects depends on the cuts of the variables shown in table 4.1; however it was estimated that for the typical values used in this analysis the

contribution to the final spectrum is at most 6% of the total reconstructed yield. Since the IMS is likely to be dominated by the background, this number is negligible.

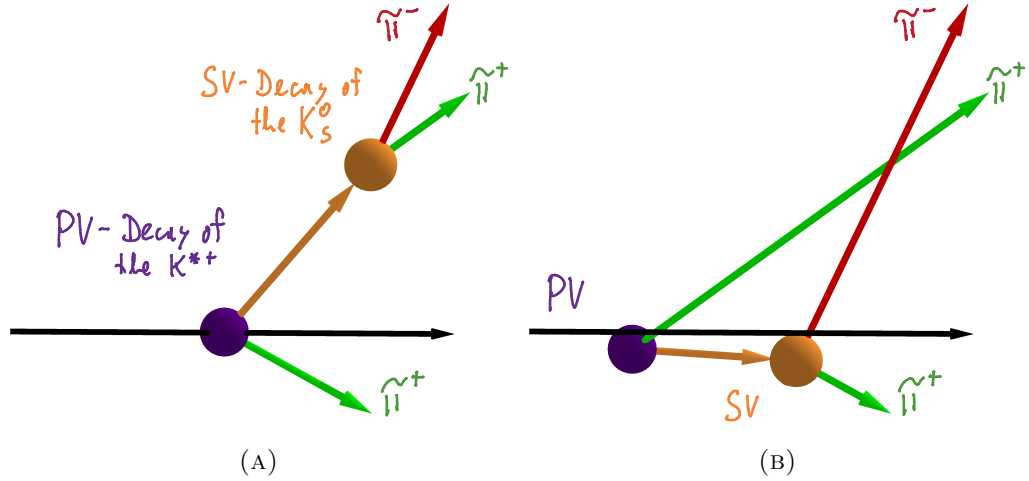


FIGURE 4.2: The same triplet of pions can sometimes be reconstructed in two different ways. This example is from a real event, the visualization was performed using GeoGebra [11].

The analysis was computationally divided into two stages. The first stage was the iteration over all available events and the reconstruction of the K^{*+} candidates with the default cuts. This part is computationally expensive and thus performed on a local batch-farm. After filtering out many of the tracks the rest of the data sample was small enough in order to be processed on local machines.

4.3.2.2 Additional cuts

The next step is to reconstruct the invariant mass spectra (IMS) of the K_S^0 and K^{*+} candidates. The IMS is the yield of the particle as a function of its reconstructed invariant mass. In the following plots the cuts have been further refined (see table 4.2).

Observable	Cut
z_{PV}	$\in (-70; -10)$ mm
$d_{xy,PV}$	< 8.5 mm
$\text{IM}(K_S^0)$	$\in (485; 505)$ MeV
d_V	> 28 mm
$\delta_{\pi^+\pi^-}$	< 13 mm
$d_{\pi^+/-}^{K^0}$	> 8.2 mm
$d_{\pi^+}^{K^*}$	< 5.6 mm

TABLE 4.2: Selection criteria used for creating figures 4.3, 4.4 and 4.5. The cut on $\text{IM}(K_S^0)$ is applied only to fig. 4.5

Figure 4.3 represents the IMS of K_S^0 particles. As can be seen there is a very strong signal corresponding to the K_S^0 meson around its nominal mass of 497.6 MeV. Obviously the events left and right from the observed peak are mostly background. Thus a cleaner IMS of K^{*+} can be obtained by applying an additional constrain to $\text{IM}(K_S^0)$. Figure 4.4 shows the invariant mass spectrum of K^{*+} without the additional cut on $\text{IM}(K_S^0)$, whereas in figure 4.5 the cut has been applied.

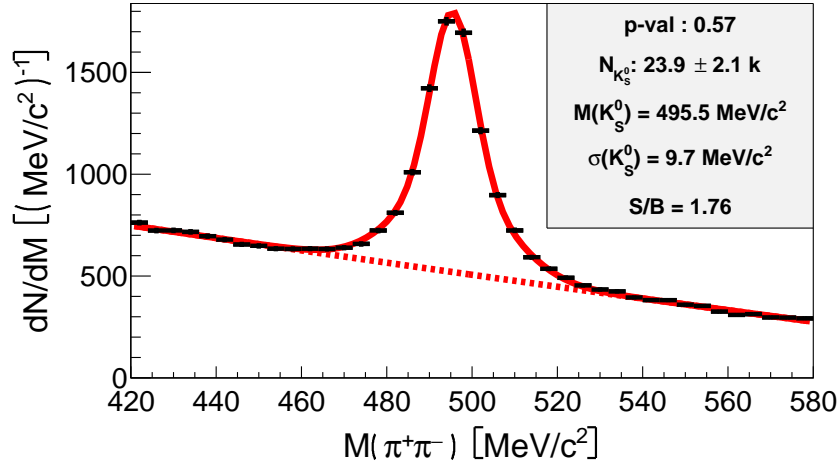


FIGURE 4.3: IMS of K_S^0 . The signal is fitted using a double-Gaussian function and the background is represented by a 3rd-degree polynomial.

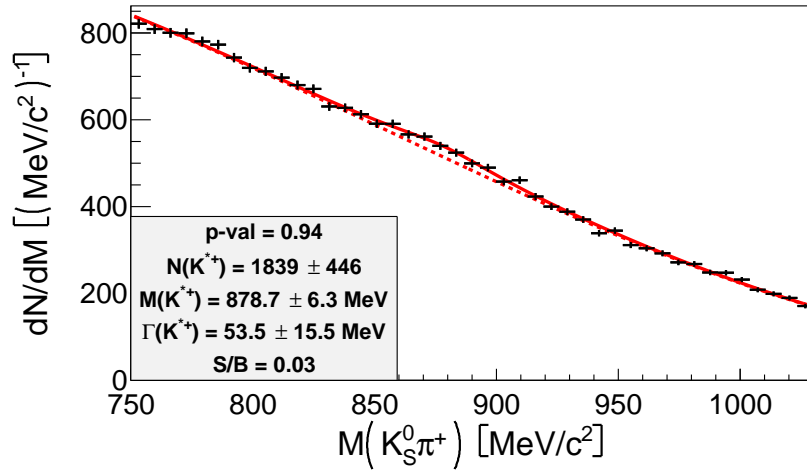


FIGURE 4.4: IMS of K^{*+} without a cut on $\text{IM}(K_S^0)$. The signal is fitted using a Breit-Wigner function and the background is represented by a 3rd-degree polynomial.

Obviously the signal-to-background ratio (S/B) is much higher in the latter case. The estimated statistics is about 2000 K^{*+} particles. It is interesting to note that the fit with the additional cut seems to produce higher uncertainties. This might be related to a poor choice of the fitting function. In the plots presented so far the signal has been modeled by a Breit-Wigner function. This function is commonly used to model resonances but it

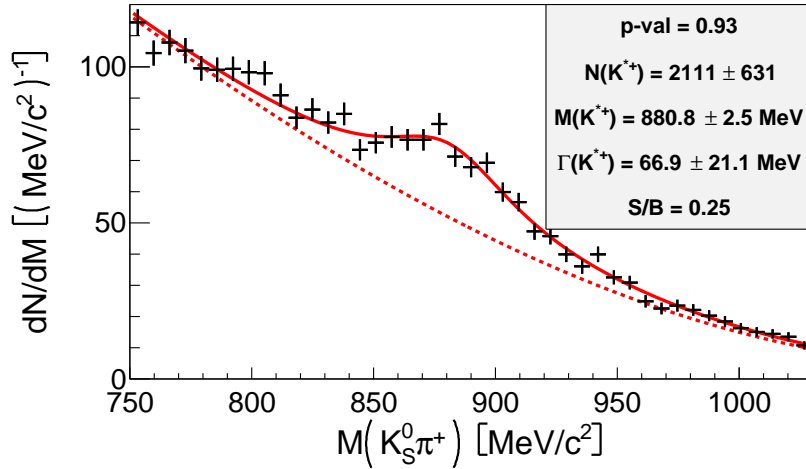


FIGURE 4.5: IMS of K^{*+} with a cut on $IM(K_S^0)$. The signal is fitted using a Breit-Wigner function and the background is represented by a 3-rd degree polynomial.

carries no additional information about phase-space limitations or detector resolution. Thus it is only a crude first-attempt to fit the signal; a more sophisticated model for the signal shape will be presented in the next sections.

4.3.3 Description of the signal

In the previous chapter the fits were performed using a straightforward approach to resonances - the Breit-Wigner function. However K^{*+} is a pretty broad resonance ($\Gamma \approx 51$ MeV) and the excess energy of the most favorable production channel (see table 1.1) is 231 MeV. This number is comparable to the width, therefore one could expect some changes in the functional shape of the signal. Additionally, since K^{*+} decays to $K^0 + \pi^+$ there is a limit on the minimal invariant mass, which is equal to the sum of the masses of the daughter particles, i.e.

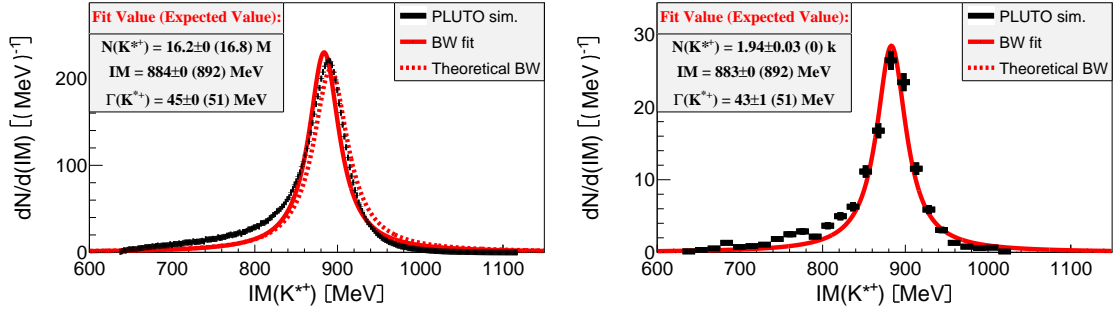
$$IM(K^{*+})_{\min} = M(K^0) + M(\pi^+) = (497.6 + 139.6) \text{ MeV} = 637.2 \text{ MeV}. \quad (4.1)$$

A detailed proof of the statement above can be found in appendix B.

In summary: the phase space for the $IM(K^{*+})$ is limited both below and above the nominal mass of the particle. Hence the functional shape of the IMS is expected to deviate a bit from the typical Breit-Wigner shape. Furthermore the limited resolution of the detector, which is expected to be in the order of 10%, might smear the signal. Therefore the effects of both the phase space limitation and the detector resolution should be investigated in more detail.

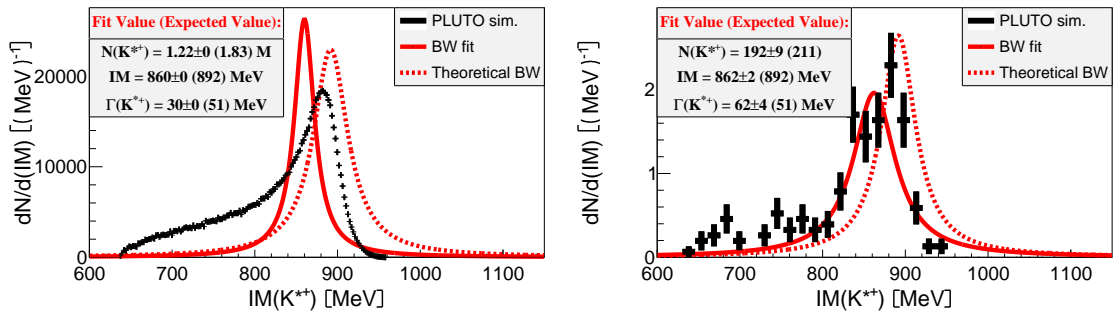
4.3.3.1 Phase space effects

Let us first examine the effect on the phase space limitations. This can be very easily probed by our phase space simulations (PLUTO). The mass of the simulated K^{*+} and the Breit-Wigner fit to those data are plotted in fig. 4.6a. Obviously there is some discrepancy between them. It could be argued that for less statistic this effect will be “lost” due to the higher uncertainty. However as can be seen in fig. 4.6b, even with a simulated yield of only 2000 K^{*+} particles the fit still cannot match the $\text{IM}(K^{*+})$ and $\Gamma(K^{*+})$ values within uncertainties. The discrepancy between the fit and the data becomes extremely strong in some particular phase-space regions. Thus during the differential analysis some of the selected bins can surely have a very distorted spectral shape. An example, based on a $p_T > 470$ MeV cut, is shown in figure 4.7.



(A) Enhanced statistics containing a total of 16.8 M events. (B) Realistic statistics containing a total of 2000 events.

FIGURE 4.6: The IMS of K^{*+} in a PLUTO simulation of the Λ -channel. All events are plotted.



(A) Enhanced statistics containing a total of 16.8 M events. (B) Realistic statistics containing a total of 2000 events.

FIGURE 4.7: The IMS of K^{*+} in a PLUTO simulation of the Λ -channel. Only events with $p_T > 470$ MeV are plotted.

The IM-cutoff at 637.2 MeV is clearly visible in figures 4.6 and 4.7. Another noticeable feature is the suppressed yield at high invariant masses and the presence of an

upper limit, which is determined by the excess energy. For the full-range plot (fig. 4.6) this should correspond to $M(K^{*+}) + \varepsilon(\Lambda\text{-channel}) \approx (892 + 231) \text{ MeV} = 1123 \text{ MeV}$. In the case of a $p_T > 470 \text{ MeV}$ cut (fig. 4.7) the analytical calculation of the maximum $\text{IM}(K^{*+})$ is somewhat more complicated (see appendix B) but the result is 960 MeV and it seems to be consistent with the simulation.

Correction for those effects

A relatively straightforward way to take those effects into account is to divide the observed spectrum by a perfect BW spectrum of the same yield. This is done by simulating with PLUTO the same reaction and the same number of events, but at much higher beam energy (23 MeV). In figure 4.8 one can see that the distribution provided by this high-energy simulation is described really well by a BW function and in fig. 4.9 one can see that the ratio between the actual and the high-energy distribution can be modeled by a second-degree polynomial with a sharp cut-off at 637.2 MeV. Below this value the yield is assumed to be zero. In addition, there is one more cut-off at higher energies. The exact value depends on the minimal allowed momenta of K^{*+} . However in the calculations here this value is approximated with the root of the second-degree polynomial. If the polynomial does not have a root its minimum is taken as the cut-off value instead. The correction function (eq. 4.2) will be referred to as the Phase Space correction Function (PSF).

$$\begin{aligned} \text{Signal} &= \text{Amplitude} \times \text{PSF} \times \text{Breit-Wigner} = \\ &= A \cdot (1 + p_1 \cdot m_{K^{*+}} + p_2 \cdot m_{K^{*+}}^2) \cdot \text{BW}(m_{K^{*+}}, \Gamma) \end{aligned} \quad (4.2)$$

The phase-space correction has to be applied independently for each kinematic bin.

4.3.3.2 Detector resolution

Another effect that needs to be investigated for its influence on the spectral shape of the $\text{IM}(K^{*+})$ is the detector resolution. The HADES momentum resolution is of the order of 5%. The K^{*+} is reconstructed using three pion tracks and thus the uncertainty will definitely grow. A very simple way of getting an estimation of the strength of the effect is to simulate, using PLUTO, K^{*+} particles with no spread in the IM, i.e. let $\Gamma \rightarrow 0$. After that HGeant can simulate the response of the detector and produce an IMS, which ideally should be a δ -function around the nominal K^{*+} mass. However, as

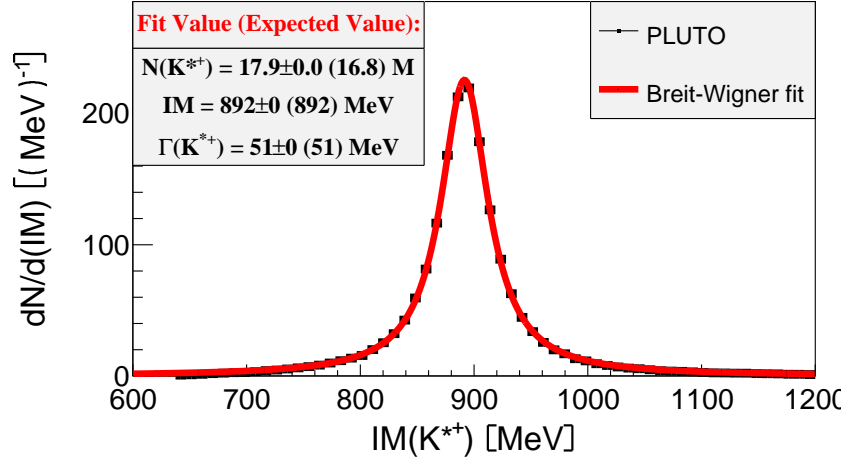


FIGURE 4.8: The IMS of K^{*+} in a PLUTO simulation of the Λ -channel using higher beam energy. According to the BW fit the yield is overestimated. However the yield is given by integrating the whole distribution, if the integration is performed only within the actual range of the observed resonance, i.e. (637, 1123) MeV, the yield becomes 16.7 ± 0.0 , which is less than 0.5% deviation from the expected value.

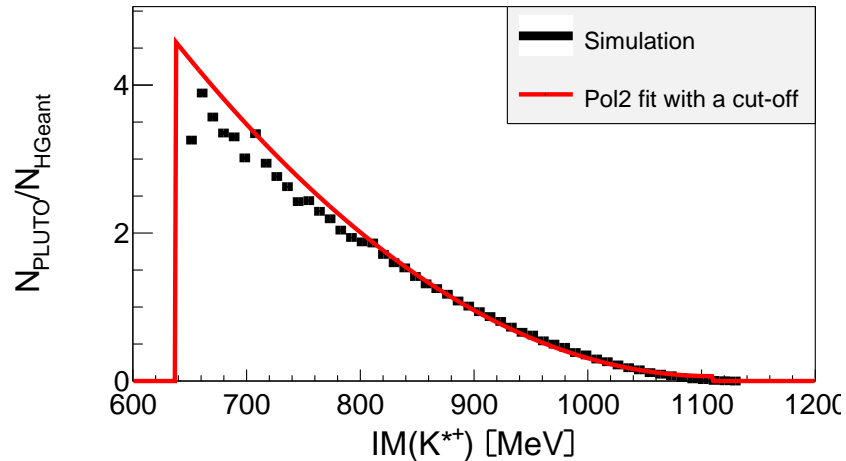
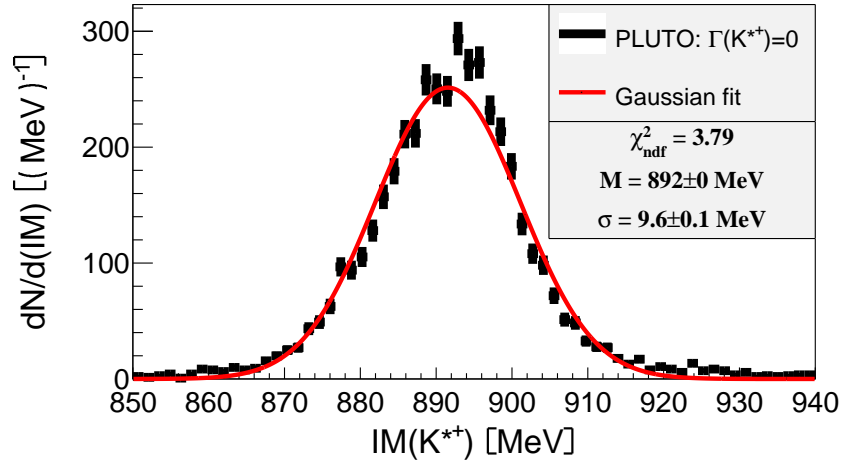


FIGURE 4.9: The phase space correction function (PSF) obtained by fitting the divided spectrum of 23 GeV PLUTO simulation (fig. 4.8) and the 3.5 GeV PLUTO simulation (fig. 4.6a).

shown in figure 4.10, this is not the case as the spectral shape of the IM has approximately a Gaussian profile with spread of ≈ 10 MeV. This number roughly corresponds to the HADES resolution of the $IM(K^{*+})$. The resolution might depend on some of the topological cut and most certainly depends on the momenta of the daughter pions. However this simple plot highlights an issue that needs to be addressed - since the detector resolution is of the same order as the width of the particle, the BW spectral shape will be smeared out by the Gaussian-distributed resolution (e.g. see fig. 4.11). Hence a much better choice to model the signal will be a convolution of a Breit-Wigner and a Gaussian profile - the Voigt function. Compared to the Breit-Wigner function, which has

FIGURE 4.10: $IM(K^{*+})$ assuming a zero width.

three input parameters: amplitude, mean value and width (Γ), the Voigt function has an additional parameter that corresponds to the standard deviation (σ) of the Gaussian profile.

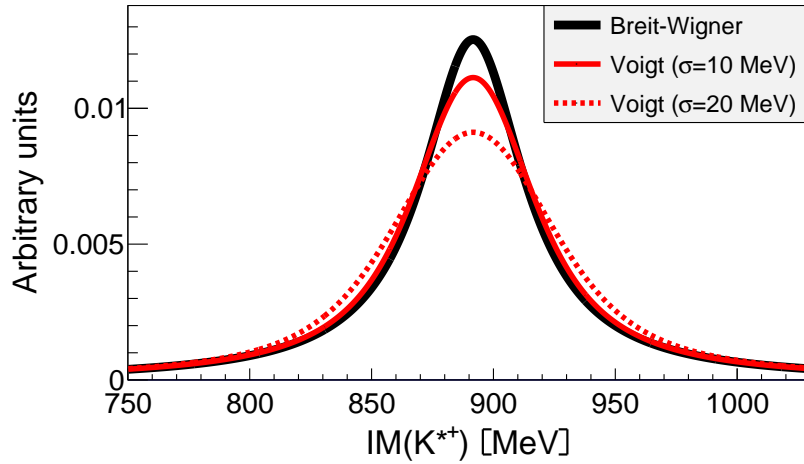


FIGURE 4.11: Plotted are one Breit-Wigner (black line) and two different Voigt functions (red lines) with mean values and widths (Γ) corresponding to the nominal values for the K^{*+} particle. The yields (integrals) of the two Voigt functions are equal to the yield of the BW function. However due to the smearing effect of the underlying Gaussian profile their spectral shapes are broadened and the maximum amplitudes lowered.

4.3.3.3 Fitting function

Analytical representation

Summarizing the previous section: a resonance is modeled by a Breit-Wigner shaped

IM. However due to phase-space limitations this shape has to be modified by a second-degree polynomial. In addition, the limited resolution causes a smearing of the signal, thus further modifying the spectral shape to a Voigt function.

The background of the IMS mostly results from analysis artifacts, such as combinatorics and misidentifications. Therefore it is reasonable to try the most trivial description of the background - a polynomial function. The degree of the polynomial should be as low as possible in order to constrain the number of free parameters and to obtain a robust fitting procedure. The function of choice in this analysis has the following analytical representation:

$$\begin{aligned} F(M_{\text{inv}}; N, M, \Gamma, \sigma) &= \text{Signal}(M_{\text{inv}}; N, M, \Gamma, \sigma) + \text{Background}(M_{\text{inv}}) = \\ &= \mathcal{N}(N) \times \mathcal{P}^{(2)}(M_{\text{inv}}) \times \text{Voigt}(M_{\text{inv}}; N, M, \Gamma, \sigma) + \mathcal{P}^{(3)}(M_{\text{inv}}), \end{aligned} \quad (4.3)$$

where

$$\begin{aligned} N &= \text{number of } K^{*+} \text{ candidates,} \\ M &= \text{mass of } K^{*+}, \\ M_{\text{inv}} &= \text{IM of the } K^{*+} \text{ candidate,} \\ \Gamma &= \text{natural width of the particle,} \\ \sigma &= \text{the standard deviation of the convoluted Gaussian,} \\ \mathcal{N} &\text{ is a normalization factor } \propto N, \\ \mathcal{P}^{(2)} &\text{ is a 2nd order polynomial (PSF)}^2, \\ \mathcal{P}^{(3)} &\text{ is a 3rd order polynomial (background).} \end{aligned} \quad (4.4)$$

It is important to note that once the IMS is fitted the extraction of the K^{*+} yield can be done by integrating the signal function only (the blue-colored part of equation 4.3).

A minor imperfection in this choice of function is the fact that it applies the smearing effect to the BW profile before being corrected for phase-space effects. The reason to use this function despite of this is two-fold. First, smearing out a polynomial is a numerical nightmare that will complicate and slow down the analysis code. Second and most important, the amount of statistics available for this analysis is not that large, which introduces a lot of uncertainties. Thus it is only needed to refine the fitting

²WLOG the first coefficient of $\mathcal{P}^{(2)}$ can be fixed to one since the normalization is determined by \mathcal{N} , i.e $\mathcal{P}^{(2)} = 1 + p_1 \cdot M + p_2 \cdot M$

function to a point where it is stable, reproducible, and the simulated output is fitted with a reasonable accuracy. Function 4.3 was thoroughly tested and did not show any drawbacks, thus it was concluded that a further refinement is unnecessary in view of the additional complexity.

Fixed parameters

The behavior and performance of any fitting procedure strongly depends on the amount of free parameters and their initial values. The IMS is a one-dimensional function with the invariant mass (M_{inv}) as its variable. The free parameters describing the signal are the yield (N), the mass (M), width (Γ) and IM-resolution (σ) of K^{*+} as well as the two parameters defining $\mathcal{P}^{(2)}$. This means that a total of 6 parameters are used for the parametrization of the signal. The background requires four additional parameters (three for each degree of $\mathcal{P}^{(3)}$ and one normalization parameter) thus function 4.3 has a total of 10 free parameters. The two polynomial functions are used for a qualitative modeling of the phase space and the background but carry no actual physical information. This fact along with the limited statistics results in a rather chaotic fitting procedure, i.e. the algorithm will converge differently depending on the initial values of the fitting function. This is clearly unacceptable, hence it is necessary to constrain or fix some of the parameters. A more careful investigation of the fitting procedure revealed that the Γ and σ parameters are affected extremely strongly by this chaotic behavior. Thus the width Γ was fixed to the nominal PDG value of 50.8 MeV. As previously demonstrated, the PSF can be directly extracted from the PLUTO simulations (fig. 4.9). Thus the fitting procedure can be split in two: first the phase space correction is extracted directly from PLUTO and the result is used to fix the parameters of $\mathcal{P}^{(2)}$. Second, the detector resolution (σ) is extracted from the HGeant simulation by fitting the simulated yield with the signal function. One can ignore the background since the simulation contains only K^{*+} particles. In this process the PSF is fixed based on the result from PLUTO, while K^{*+} width (Γ) is fixed based on the PDG. The resulting value for the parameter σ is further used to constrain the fitting function for the experimental data. The “work-flow” of the fitting procedure is schematically represented in figure 4.12. The mass is not fixed at any point in both the simulation and the experimental data. Hence it can be used as a cross check of the accuracy of the fit. It should be noted that depending on the kinematic cuts applied to the data, the PSF and possibly σ can change! Thus it is important to always apply identical kinematic cuts on both

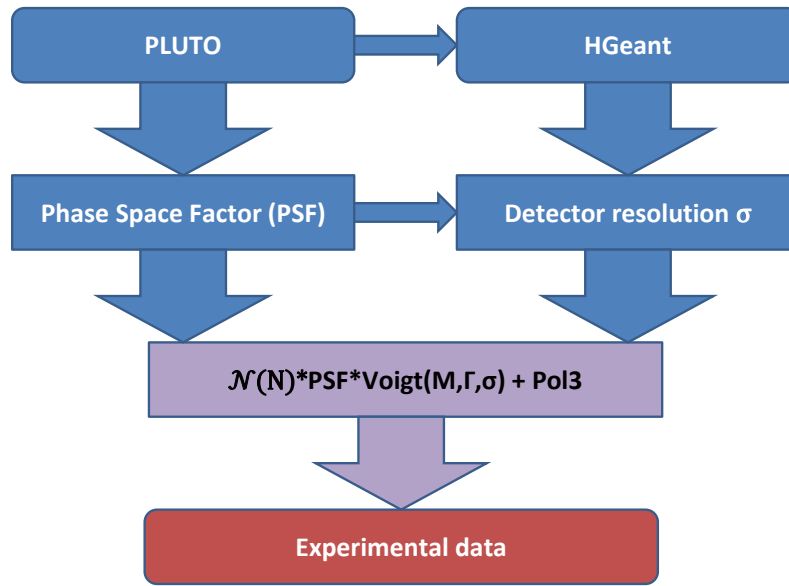


FIGURE 4.12: The data are fitted using the function 4.3. In order to constrain some of the parameters a PLUTO simulation is used to extract the PSF and feed data to a HGeant simulation with the help of which, using the PSF obtained from PLUTO and the PDG value of Γ , the detector resolution σ is extracted. Finally the PSF, Γ and σ are all being fixed and the the experimental data can be fitted.

the simulated and the experimental data. This is of course relevant for the differential analysis, which probes different regions of the phase space. An example of the extraction of σ from a HGeant IMS is shown in figure 4.13. Experimental spectra fitted with this

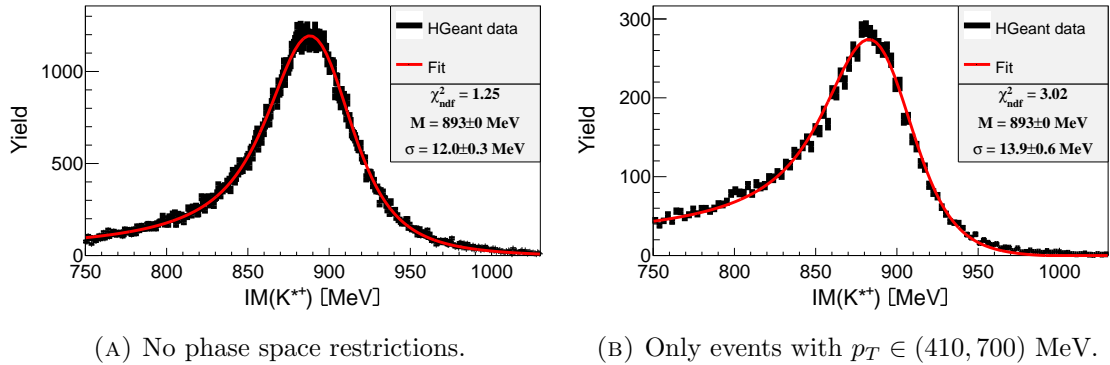


FIGURE 4.13: Extraction of σ from HGeant simulations. The phase space correction is extracted from PLUTO simulations (e.g. see fig. 4.9) and the width Γ is fixed to 50.8 MeV. The two sub-figures display different regions of the phase space. The signal seems to be well described. This example is based on an exclusive simulation of the Λ -channel.

procedure are shown in figure 4.14. The cuts used in those plots are listed in table 4.3.

Observable	Restriction
z_{PV}	$\in (-70; -10)$ mm
$d_{xy,PV}$	< 8.5 mm
$\text{IM}(K_S^0)$	$\in (485.8, 505.2)$
d_V	> 28 mm
$\delta_{\pi^+\pi^-}$	< 13 mm
$d_{\pi^+/-}^{K^0}$	> 8.2 mm
$d_{\pi^+}^{K^*}$	< 5.6 mm

TABLE 4.3: List of the commonly used cuts in this work.

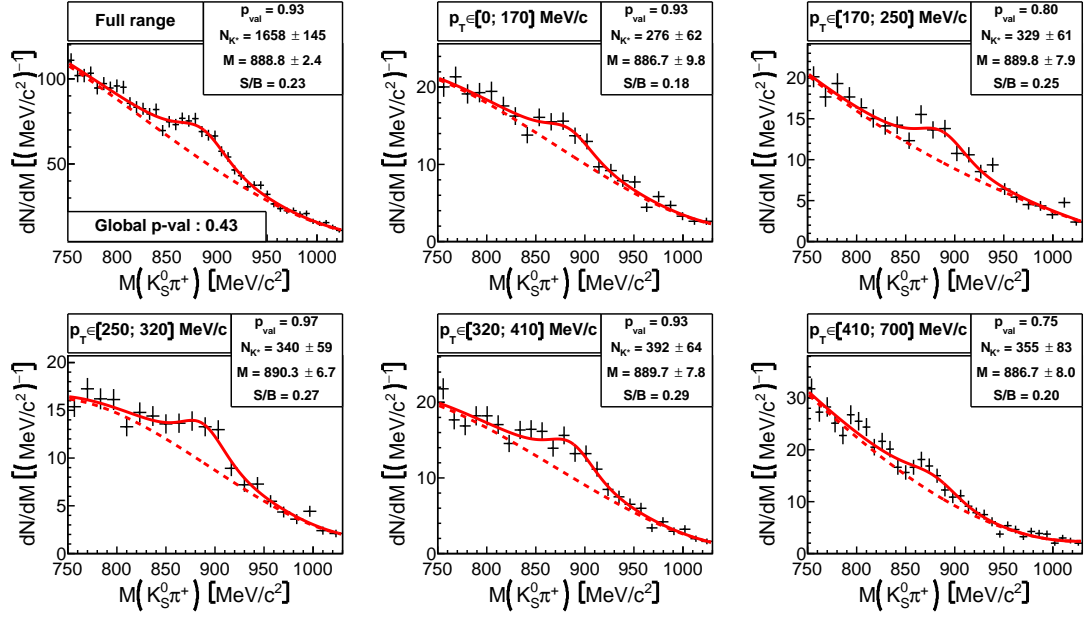


FIGURE 4.14: Experimental IMS of K^{*+} . The spectra are fitted using the procedure described in this chapter, i.e. the fitting function is given by equation 4.3 and the PSF, Γ and σ are fixed based on simulations. Each plot represents a different region of the phase-space. The black crosses represent the data (with uncertainties), the solid red lines are the full fit functions and the dashed red lines represent the corresponding backgrounds.

4.3.4 Correction for acceptance and efficiency

The experimental yield needs to be corrected for acceptance and efficiency effects. As previously explained (see chapter 2.3) a differential analysis is needed in order to achieve that. From the data shown in figure 4.14 one can conclude that the number of K^{*+} particles is less than 2000 and that it is not reasonable to divide the full yield into more than 5-6 bins. The possibility of extending the number of bins was tested, but unfortunately the fitting function seemed to lose its sensibility and reliability for higher bin numbers. For this reason it was concluded to divide the data in up to 5

bins and perform a single-differential analysis. Unfortunately this can introduce some integrated effects in each bin, unless the phase-space simulation accurately models the production. A very simple but effective model of the phase space is to take into account the two dominating production channels: $p + p \rightarrow p + \Lambda + K^{*+}$ (Λ -channel) and $p + p \rightarrow p + \Sigma^0 + K^{*+}$ (Σ -channel) and use a mixture of those for the AEC. The possibility of any anisotropic production is still not included. The assumption that the production is not highly anisotropic can in fact be justified just by considering the results presented in figure 4.14. In this plot the full phase-space spectrum produces a total yield of 1658 ± 145 particles and the total integrated yield, i.e. the sum of the yields from the p_T restricted spectra, is 1692 ± 148 . Those two numbers are fully compatible within the uncertainties and therefore the assumption for predominantly an isotropic production is justified. However this argumentation is not enough to exclude anisotropic production. For this reason the whole analysis procedure was repeated multiple times using a different kinematic observable for the differential analysis on each re-iteration. The selected observables are the transverse momentum (p_T), the center of mass momentum (p_{CM}), the rapidity (Y) and the center of mass cosine theta ($\cos\theta_{CM}$) of the K^{*+} particle. The assumption about a relatively isotropic production is justified, as long as the results from the different runs are self-consistent.

4.3.4.1 The two-channel model

A problem regarding the two-channel production model is that the exact contribution of each channel is unknown. Thus the cross sections ratio, which corresponds to the yield ratio, between the two channels should be implemented as an additional analytical parameter. Before focusing on this issue let first of all examine the mathematical properties of this model. Generally (see eq. 2.17 and chapters 2.3 and 3.4) the correction is given by:

$$C_i^{(2ch)} = \frac{N_i^{(2ch)}}{n_i^{(2ch)}}, \quad (4.5)$$

where i represents the bin number and $N_i^{(2ch)}$ and $n_i^{(2ch)}$ are defined according to the notation rules described in table 4.4. By combining equations 4.5 and 2.18 one obtains:

$$N_i^{(exp)} = C_i^{(2ch)} n_i^{(exp)} = \frac{N_i^{(2ch)}}{n_i^{(2ch)}} n_i^{(exp)} \quad (4.6)$$

Notation	Meaning
$N_i^{(X)}$	The total corrected yield of the i^{th} bin in the data sample X .
$n_i^{(X)}$	The reconstructed uncorrected yield of the i^{th} bin in the data sample X .
$X = \text{exp}$	Experimental data.
$X = \Lambda, \Sigma$	Simulated data for the Λ and Σ channel respectively.
$X = \text{2ch}$	Simulated data for the two-channel model.
$w^{(\Lambda)}, w^{(\Sigma)}$	Weight of the contribution of the respective channel to the two-channel model.
$p^{(\Lambda)}, p^{(\Sigma)}$	Contribution (percentage) of the respective channel to the total two-channel sample.

TABLE 4.4: Notation rules used for the AEC.

$N_i^{(2\text{ch})}$ can be defined as:

$$N_i^{(2\text{ch})} := w^{(\Lambda)} N_i^{(\Lambda)} + w^{(\Sigma)} N_i^{(\Sigma)}, \quad (4.7)$$

where $w^{(\Lambda)}$ and $w^{(\Sigma)}$ represent the weight factors of the pure Λ and Σ channel respectively. If such a sample is used as an input for HGeant it is expected that:

$$n_i^{(2\text{ch})} := w^{(\Lambda)} n_i^{(\Lambda)} + w^{(\Sigma)} n_i^{(\Sigma)} \quad (4.8)$$

number of K^{*+} candidates will be reconstructed. Thus equation 4.5 can be rewritten as:

$$C_i^{(2\text{ch})} = \frac{w^{(\Lambda)} N_i^{(\Lambda)} + w^{(\Sigma)} N_i^{(\Sigma)}}{w^{(\Lambda)} n_i^{(\Lambda)} + w^{(\Sigma)} n_i^{(\Sigma)}}. \quad (4.9)$$

The K^{*+} yield in PLUTO and HGeant is known for both the Λ and the Σ channels. The only unknowns in equation 4.9 are the weight factors $w^{(\Lambda)}$ and $w^{(\Sigma)}$. They can be determined up to a constant from the ratio R between the Λ -associated and Σ -associated kaons:

$$R := \frac{w^{(\Lambda)} N^{(\Lambda)}}{w^{(\Sigma)} N^{(\Sigma)}}, \quad (4.10)$$

where $N^{(\Lambda)} = \sum_i N_i^{(\Lambda)}$ and $N^{(\Sigma)} = \sum_i N_i^{(\Sigma)}$ are the total numbers of input kaons for HGeant associated to the corresponding channel. This representation (equations 4.9 and 4.10) is especially useful since it highlights the possibility to calculate the correction coefficient $C_i^{(2\text{ch})}$ for any desired ratio R , as long as one of the weight coefficients w is

fixed, only by using the existing simulation data of the pure Λ - and the pure Σ -channel production. Thus there is no need for performing any additional simulations. The simulated PLUTO yield in both channels is 2 million³ K^{*+} particles. In order to have a consistent error calculation, a further requirement is that $N^{(2\text{ch})} = N^{(\Lambda)} = N^{(\Sigma)} = 2 \cdot 10^6$. This condition ensures that $w^{(\Lambda)} = p^{(\Lambda)}$ and $w^{(\Sigma)} = p^{(\Sigma)}$. Thus equation 4.5 is further simplified to:

$$C_i^{(2\text{ch})} = \frac{N_i^{(2\text{ch})}}{n_i^{(2\text{ch})}} = \frac{p^{(\Lambda)} N_i^{(\Lambda)} + p^{(\Sigma)} N_i^{(\Sigma)}}{p^{(\Lambda)} n_i^{(\Lambda)} + p^{(\Sigma)} n_i^{(\Sigma)}}, \quad (4.11)$$

with

$$p^{(\Lambda)} + p^{(\Sigma)} = 1. \quad (4.12)$$

Equation 4.12 removes a further degree of freedom to the weight coefficients w , meaning that $C_i^{(2\text{ch})}$ can be calculated for any desired ratio R . The corrected yield is obtained from eq. 4.6 and 4.11:

$$N_i^{(\text{exp})} = C_i^{(2\text{ch})} n_i^{(\text{exp})} = \frac{p^{(\Lambda)} N_i^{(\Lambda)} + p^{(\Sigma)} N_i^{(\Sigma)}}{p^{(\Lambda)} n_i^{(\Lambda)} + p^{(\Sigma)} n_i^{(\Sigma)}} n_i^{(\text{exp})}. \quad (4.13)$$

The next logical step is to find optimal values for $p^{(\Lambda)}$ and $p^{(\Sigma)}$. To achieve this, one needs to use the property that under ideal conditions, i.e. a correct model and a perfect simulation, the detected yield in each bin should equal the simulated yield up to a normalization constant:

$$n_i^{(\text{exp})} = \mathcal{N} n_i^{(2\text{ch})} \quad \forall i, \quad (4.14)$$

where $\mathcal{N} = n_{\text{tot}}^{(\text{exp})} / n_{\text{tot}}^{(2\text{ch})}$. The optimal values for $p^{(\Lambda)}$ and $p^{(\Sigma)}$ can be determined by performing a χ^2 minimization of the bin-wise yield distributions in simulation and in experiment. Mathematically this corresponds to calculating:

$$\min \left\{ \sum_i \left[\frac{n_i^{(\text{exp})} - n_i^{(2\text{ch})}}{\sigma(n_i^{(\text{exp})} - n_i^{(2\text{ch})})} \right]^2 \right\}, \quad (4.15)$$

where the minimization is performed over different values for $p^{(\Sigma)}$. The data did not show any strong dependence on this parameter, thus the minimization was performed by scanning the data in $p^{(\Sigma)}$ steps of 0.1. After applying some systematic checks, which will be explained in chapter 4.3.6, the final value of $p^{(\Sigma)}$ for the p_T observable was found to be

³Actually a total of 16Mi events were simulated and used as an input for HGeant. The reason why only 2M events were accessed is explained in appendix C.

$0.41^{+0.19}_{-0.22}$. Figure 4.15 shows the uncorrected yield as a function of p_T compared to the simulated yields (after HGeant) for 0%, 41% and 100% Σ -channel contribution. All of the scenarios produce reasonable χ^2 values, but clearly the 41% Σ -channel contribution gives the best description of the data, and the 100% Σ -channel contribution the worst. This is expected, since the Λ -channel is energetically more favorable as compared to the Σ -channel (see table 1.1). Furthermore the assumption that all other production

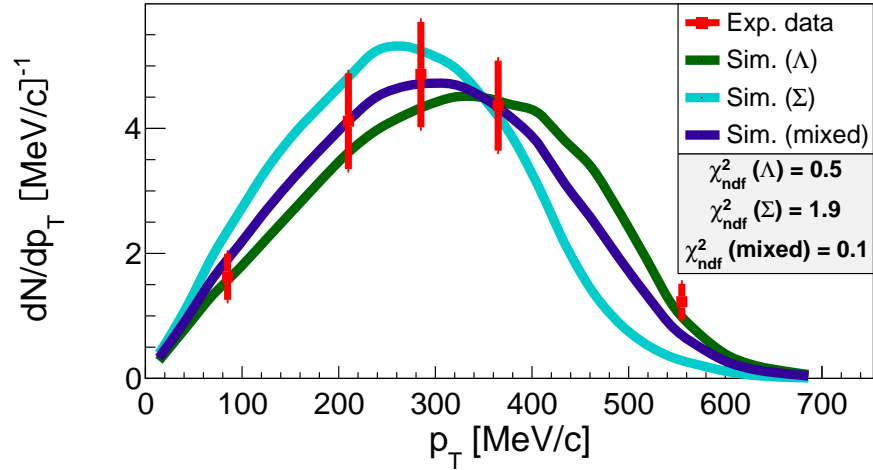


FIGURE 4.15: Uncorrected p_T spectrum of K^{*+} obtained by plotting the yield of each p_T bin (see fig. 4.14) and dividing it by the bin width, i.e. the p_T range. The expected values as obtained from the HGeant output (colored lines) are plotted in addition to the experimental results (red bars). The three different curves represent different Σ -channel contributions. The total yield of each model is normalized to the total experimental yield. Spectra obtained from other observables can be found in appendix D.

channels can be neglected (see chapter 4.2) is proven to be correct. This can be explained by using only the energy and momentum conservation. If more energy is used for the production process and transferred to particles other than K^{*+} , K^{*+} itself will possess a lower kinetic energy and, naturally, a lower momentum. Thus the p_T spectrum will be shifted towards lower values, as in the case of the Σ -channel (see fig. 4.15).

4.3.4.2 Branching ratios

After the AEC coefficients are sorted out, the next step is to use equation 4.13 to extract the actual K^{*+} yield. However, the analysis procedure is sensitive only to K^{*+} decaying into $K_S^0 + \pi^+$. For this reason a correction using equation 4.13 can provide only the yield associated with this particular decay of K^{*+} . As mentioned in chapter

1.2.3, the two main decay channels are:

$$K^{*+} \rightarrow K^0 + \pi^+ \quad \text{and} \quad K^{*+} \rightarrow K^+ + \pi^0. \quad (4.16)$$

The K^0 particle is a mixture between the two weak eigenstates K_S^0 and K_L^0 (see appendix A) and the ratio between the yields of the two is 1:1. This analysis relies on reconstructing the K^{*+} exclusively from a $K_S^0 + \pi^+$, hence only a half of the total K^{*+} yield associated with a decay into $K^0 + \pi^+$ is reconstructed. The next question is what is the branching ratio between the two decay channels shown in 4.16. This can be read-out from the table of the Clebsch-Gordan coefficients (see e.g. [10]) by using the information on the isospin configuration of the daughter particles and the decay products. The K^{*+} particle can be expressed as a combination of two distinct final-states, each containing two particles. Mathematically this is expressed as:

$$|I I_3\rangle = \sum_x C^{(x)} \left| I^{(x_1)} I_3^{(x_1)} \right\rangle \left| I^{(x_2)} I_3^{(x_2)} \right\rangle, \quad (4.17)$$

where x are the possible final states in which the initial state $|I I_3\rangle$ is decomposed into, x_1 and x_2 are the two particles of which the final state x is composed, $C^{(x)}$ are the corresponding Clebsch-Gordan coefficients and I and I_3 stand for the isospin and the third component of the isospin respectively. In this particular case:

$$\begin{aligned} x &\in \{K_S^0 \pi^+, K^+ \pi^0\}, \\ x_1 &\in \{K_S^0, K^+\}, \\ x_2 &\in \{\pi^+, \pi^0\}, \end{aligned} \quad (4.18)$$

and hence:

$$\begin{aligned} |I I_3\rangle_{K^{*+}} &= C^{(K_S^0 \pi^+)} \left| I^{(K_S^0)} I_3^{(K_S^0)} \right\rangle \left| I^{(\pi^+)} I_3^{(\pi^+)} \right\rangle + \\ &+ C^{(K^+ \pi^0)} \left| I^{(K^+)} I_3^{(K^+)} \right\rangle \left| I^{(\pi^0)} I_3^{(\pi^0)} \right\rangle. \end{aligned} \quad (4.19)$$

The square of the Clebsch-Gordan coefficients represents the probability to decay via the respective channel and the branching ratio is given as:

$$\text{Branching Ratio} = \left| C^{(K_S^0 \pi^+)} \right|^2 : \left| C^{(K^+ \pi^0)} \right|^2. \quad (4.20)$$

Using the isospin properties of the particles involved (see table 4.5) equation 4.19 becomes:

$$\left| \frac{1}{2} \frac{1}{2} \right\rangle_{K^{*+}} = C^{(K_S^0 \pi^+)} \left| \frac{1}{2} - \frac{1}{2} \right\rangle |1 \ 1\rangle + C^{(K^+ \pi^0)} \left| \frac{1}{2} \frac{1}{2} \right\rangle |1 \ 0\rangle. \quad (4.21)$$

Figure 4.16 shows the relevant part of the Clebsch-Gordan table and one can read out

Particle	I	I_3
K^{*+}	1/2	1/2
K_S^0	1/2	-1/2
π^+	1	1
π^0	1	0

TABLE 4.5: Isospin properties.

that $C^{(K_S^0 \pi^+)} = \sqrt{2/3}$ and $C^{(K^+ \pi^0)} = -\sqrt{1/3}$. Thus it can be concluded (see eq. 4.20) that the branching ratio between $K^{*+} \rightarrow K^0 + \pi^+$ and $K^{*+} \rightarrow K^+ + \pi^0$ is 2:1, i.e. 2/3 of all K^{*+} particles decay via the $K^{*+} \rightarrow K^0 + \pi^+$ channel. Summarizing the above

$1 \times 1/2$	$3/2$	$3/2$	$1/2$		
$+1 \ +1/2$	$+3/2$	1	$+1/2 \ +1/2$		
$+1 \ -1/2$	$0 \ +1/2$	$1/3$	$2/3$	$3/2$	$1/2$
		$2/3$	$-1/3$	$-1/2$	$-1/2$
		$0 \ -1/2$	$-1 \ +1/2$	$2/3$	$1/3$
				$1/3$	$-2/3$
				$-1 \ -1/2$	$3/2$
					1

FIGURE 4.16: Clebsch-Gordan coefficients [7]. Please refer to a specialized literature for a detailed explanation on how to read the table (e.g. [10]). In accordance with the notation in equation 4.17, the olive box corresponds to the values of $I^{(x_1)}$ and $I^{(x_2)}$, the magenta box corresponds to the I and I_3 values of the initial state (K^{*+}), the red arrows point to the rows where $I_3^{(x_1)}$ and $I_3^{(x_2)}$ are to be found and finally in the light-green box are the corresponding Clebsch-Gordan coefficients, written without the square root sign.

discussion: 2/3 of the K^{*+} particles decay into $K^0 + \pi^+$ and 1/2 of the neutral kaons (K^0) are K_S^0 particles, thus this analysis is sensitive only to 1/3 of the total K^{*+} yield. Hence the final yield needs to be multiplied by a factor of 3 in order to take those effects into account, i.e.

$$C^{(\text{BR})} := 3, \quad (4.22)$$

and equation 4.13 can be expanded to:

$$N_i^{(\text{exp})} = C^{(\text{BR})} C_i^{(2\text{ch})} n_i^{(\text{exp})}. \quad (4.23)$$

As a final remark it is worth mentioning that K_S^0 decays into a $\pi^+ + \pi^-$ pair in 69.2% of the time. There are other decay channels, most notably the decay into a $\pi^0 + \pi^0$ pair, but there is no need to explicitly correct the yield for this effect since it is simulated by HGeant and consequently included in $C^{(2\text{ch})}$.

4.3.4.3 Extraction of the cross section

Up to this point only the absolute yield was evaluated. The physical quantity of interest is the cross section and thus it is necessary to normalize the cross section to the yield. This can be done by exploring the fact that the ratio between the cross sections of two processes is equal to the ratio between the absolute yields (eq. 4.24).

$$\frac{\sigma(K^{*+})}{N(K^{*+})} = \frac{\sigma_{\text{el}}(pp)}{N_{\text{el}}(pp)}. \quad (4.24)$$

Since the p+p elastic cross section is theoretically known and the absolute yield is measured by HADES [30], one can use this information to extract the total K^{*+} production cross section:

$$\sigma(K^{*+}) = \frac{\sigma_{\text{el}}(pp)}{N_{\text{el}}(pp)} N(K^{*+}) = C^{(\sigma)} N(K^{*+}), \quad (4.25)$$

where

$$C^{(\sigma)} := 1.11 \times 10^{-5} \mu\text{b}. \quad (4.26)$$

The value of $C^{(\sigma)}$ is determined based on [30], taking into account that this analysis uses 12164 number of files and the LVL2 condition downscales the number of events by a factor of 3. Hence, based on equations 4.23, 4.25 and 4.26 the K^{*+} production cross section can be bin-wise calculated using:

$$\sigma_i^{(\text{exp})} = C^{(\sigma)} C^{(\text{BR})} C_i^{(2\text{ch})} n_i^{(\text{exp})}. \quad (4.27)$$

The total production cross section is simply the integral of the differential distribution which in the discrete case is given by a summation over all bins:

$$\sigma_{\text{tot}}^{K^{*+}} = C^{(\sigma)} C^{(\text{BR})} \sum_i C_i^{(2\text{ch})} n_i^{(\text{exp})}, \quad (4.28)$$

4.3.5 First results

Figure 4.17 shows the results after applying equation 4.28 to the available data. Each plot represents the result after performing the differential analysis on a different kinematic observable. The results for the total production cross section are listed in

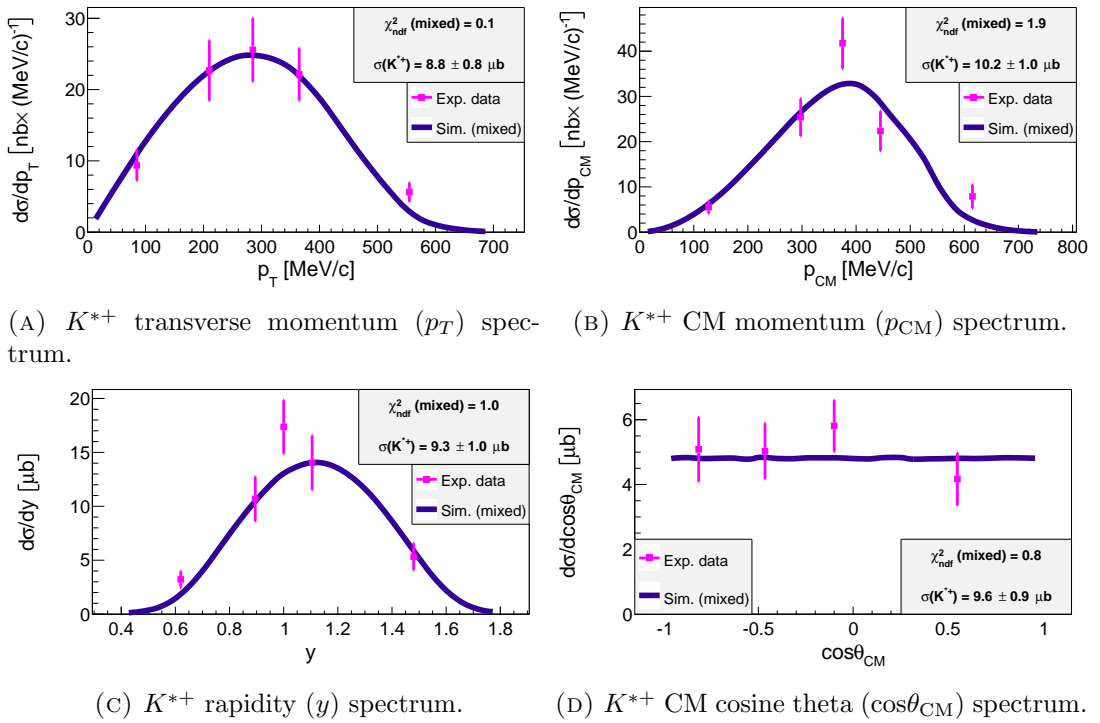


FIGURE 4.17: The corrected IMS for 4 different kinematic observables. Only statistical errors are taken into account.

table 4.6. There are some small discrepancies between the results, but they are all equal within the statistical errors. This means that the correction procedure is quite stable, despite the very coarse discretization. Herewith the assumption about an isotropic production, discussed in chapter 4.3.4, is proven to be reasonable within the uncertainties. Nevertheless the results from table 4.6 are still not finalized. An issue that has been overlooked in the discussion so far is the influence of the topological cuts (see chapter 4.3.2) on the analysis procedure. In theory, as long as all assumptions made are extremely good, there should be no influence of the topological cuts on the final result. In

Observable	$\sigma_{K^{*+}}(\mu b)$
p_T	8.8 ± 0.8
p_{CM}	10.2 ± 1.0
y	9.3 ± 1.0
$\cos\theta_{CM}$	9.6 ± 0.9

TABLE 4.6: First results for the total K^{*+} production cross section. The results are obtained by using one set of topological cuts, listed in table 4.3, and the errors represent only the statistical uncertainties.

reality this will certainly not be true, therefore it is of great importance to perform a consistency check regarding those cuts. The solution to this problem is explained in the next section.

4.3.6 Investigation of the systematic error

The systematic error is always challenging to be estimated, since there might be many different hidden sources of uncertainties. This analysis relies heavily on the topological cuts in order to get a clear K^{*+} signal. Hence it is assumed that the main source of systematic error is related to those cuts. The investigation of this particular source of uncertainty can be performed by varying the topological cuts and recalculating the K^{*+} cross section. Any deviation in the result is considered as systematic uncertainty. The setup for this study was to select 1200 different cut combinations. The selection was done according to the cut variations shown in table 4.7. Each combination was separately analyzed, for all observables of interest, by extracting the signal, i.e. fitting the relevant IMS, and performing acceptance and efficiency corrections. Before accepting the result from a single iteration certain quality assurance needs to be fulfilled. This is needed in order to reject all iterations that may have encountered some numerical problem, e.g. divergence of a fitting function. These criteria are listed in table 4.8. Figure 4.18 represents the distribution of the accepted results obtained from the 1200 combinations for each analyzed observable. The systematic uncertainty is defined as the 68% confidence central interval of this distribution. This means that the value for the cross section is the median of the distribution and the upper and lower errors are chosen in such a way, that 16% of the yield is rejected on each side of the distribution (the grayed-out areas in the plots). The reason to use the median approach and not the

Observable	Min	Max	Steps
$\text{IM}(K_S^0) \in (495.5 - X, 495.5 + X)$	$X = 1\sigma$	$X = 2\sigma$	3
d_V [mm]	> 24	> 40	5
$\delta_{\pi^+\pi^-}$ [mm]	< 7	< 13	4
$d_{\pi^+/-}^{K_S^0}$ [mm]	> 5.6	> 16	5
$d_{\pi^+}^{K^*}$ [mm]	< 3	< 16	6

TABLE 4.7: Rules for selecting the cut-combinations. The restriction on each observable changes in equal discrete steps, the first step is in the “min” column and the last step is the “max” column. The number of steps in which each observable is changed are listed in the last column. For the cut around the $\text{IM}(K_S^0)$, the invariant mass was assumed to be 495.5 MeV and the standard deviation (σ) of the distribution 9.7 MeV. These values are extracted from figure 4.3.

Conditions
No more than 1 bin failed the AE correction and was extrapolated
The covariance matrix of the global fit is positive definite
p-val (Global fit) > 0.05
Relative Error (in all non-zero bins) < 0.4

TABLE 4.8: Conditions for accepting the analysis result for a specific topological cut. A bit more details on those conditions can be found in appendix E.

more commonly used mean value and standard deviation approach is mostly due to the relatively asymmetrical distributions, which makes the standard deviation an inaccurate estimate of the error. By contrast the median approach enables the calculation of asymmetrical errors. Finally the total statistical error is calculated as the mean statistical error of all accepted iterations.

An analogous study can be performed on the Σ -channel contribution $p^{(\Sigma)}$. This is related to the discussion in section 4.3.4.1. If an optimal $p^{(\Sigma)}$ is calculated for each topological cut and added to a single distribution (fig. 4.19), from which the median and the central interval are extracted, the final result for the Σ -channel contribution will be obtained.

4.3.7 Final results

The final corrected spectra, obtained after analyzing the systematic uncertainty, are shown in figure 4.20. The final results for the total K^{*+} production cross section are summarized in table 4.9. Apparently all results are the same within the uncer-

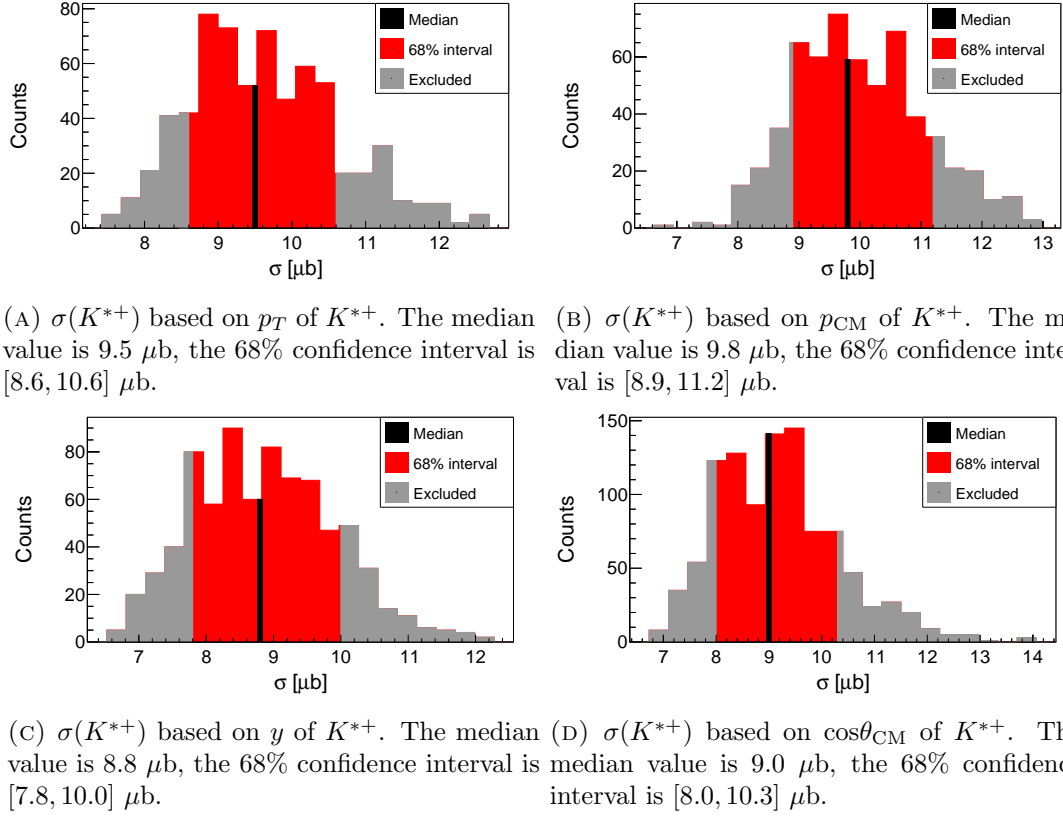


FIGURE 4.18: Systematic error of the total K^{*+} production cross section. These plots are used to obtain the final results shown in table 4.9.

Observable	$\sigma_{K^{*+}}(\mu\text{b})$
p_T	$9.5 \pm 0.9(\text{stat})_{-0.9}^{+1.1}(\text{syst})$
p_{CM}	$9.8 \pm 0.9(\text{stat})_{-0.9}^{+1.4}(\text{syst})$
y	$8.8 \pm 1.0(\text{stat})_{-1.0}^{+1.2}(\text{syst})$
$\cos\theta_{\text{CM}}$	$9.0 \pm 1.1(\text{stat})_{-1.0}^{+1.3}(\text{syst})$

TABLE 4.9: Final results for the total K^{*+} production cross section.

tainties. However, the investigated observables are dependent on each another, which makes the combination of all of the results into a single number statistically incorrect. Thus as a final result only one of the entries has to be selected. As the p_T result has the smallest error it is reasonable to use this as the final value for the cross section. Hence our **final solid statement is that the total production cross section of the $K^*(892)^+$ particle is:**

$$\sigma_{\text{tot}}(K^*(892)^+) = 9.5 \pm 0.9(\text{stat})_{-0.9}^{+1.1}(\text{syst}) \mu\text{b} \quad (4.29)$$

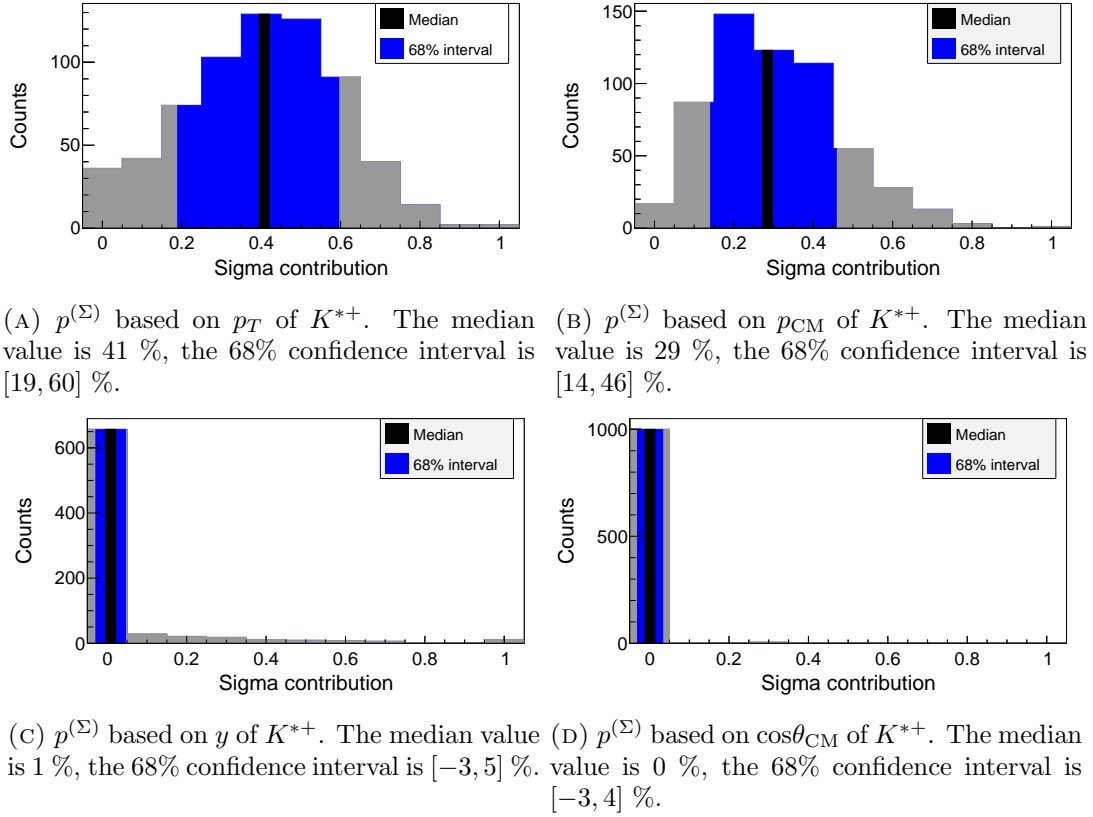
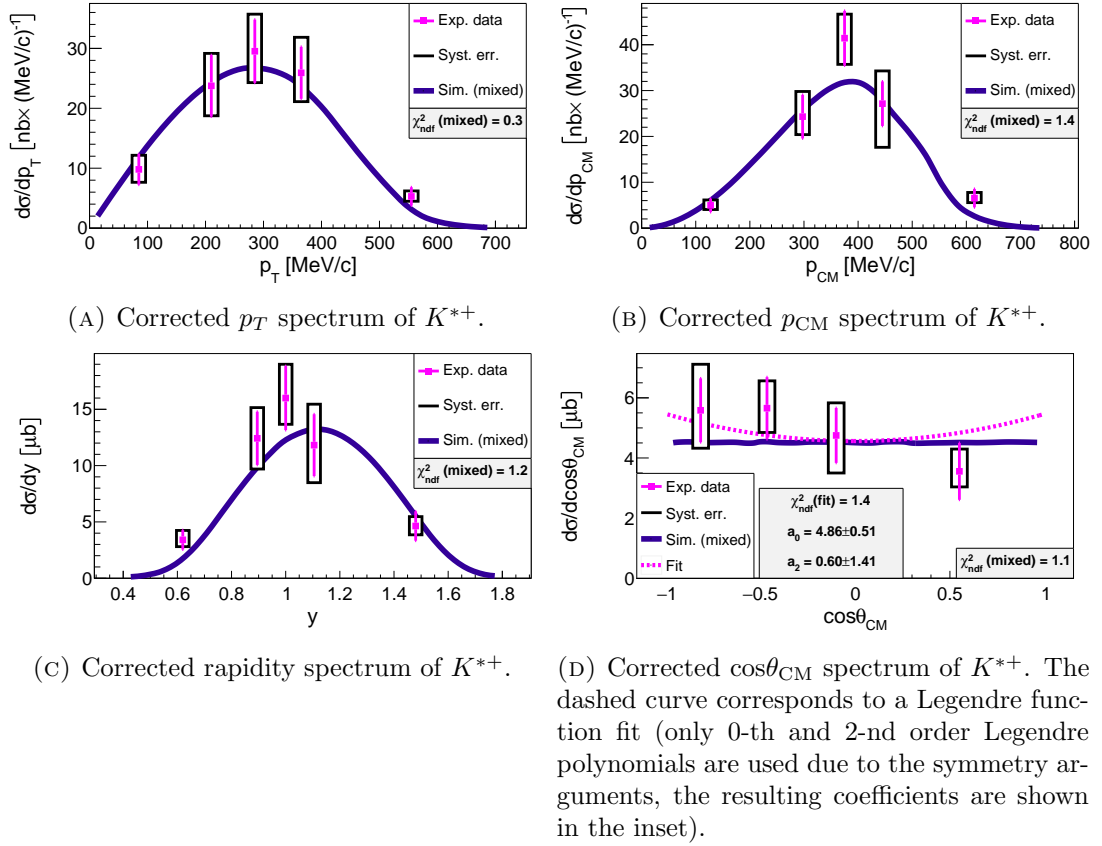


FIGURE 4.19: Systematic error of the Σ -channel contribution. Note that the results in 4.19c and 4.19d are meaningless, since the rapidity and $\cos\theta_{CM}$ observables are not a good direct probe of the phase space (see figure D.1 in appendix D). Thus the Λ - and the Σ -channel are indistinguishable from each other when analyzed using those observables. The fitting procedure is stuck around the initial values, which were set to $p^{(\Sigma)} = 0$, and the negative values in the intervals are simply binning artifacts.

An additional comment can be done regarding figure 4.20d. The phase-space simulation (the solid line) is based on an isotropic production of K^{*+} . A fit with Legendre polynomials (see appendix F) was performed to test the hypothesis of an anisotropic production. According to the obtained χ^2 values both the isotropic simulation and the anisotropic hypothesis fit to the data reasonably well. However the simulation provides a better χ^2 value which suggests that within the uncertainties it is impossible to detect any relevant anisotropy.

4.4 Spin alignment effects

The developed analysis procedure allows to perform an additional study on the K^{*+} , namely to look for spin-alignment effects, i.e. a preferred spin-orientation of the particles. The spin-alignment is characterized by a spin-density matrix ρ with elements $\rho_{mm'}$ [33].

FIGURE 4.20: Corrected spectra of K^{*+} .

The spin-density matrix possesses the property:

$$\text{Tr}(\rho) = 1. \quad (4.30)$$

Therefore the diagonal elements, which represent the probability of spin-orientation along a certain axis, are of special importance. Concentrating on the case of spin 1 particles one can define the diagonal elements as $\rho_{1,1}$, $\rho_{0,0}$ and $\rho_{-1,-1}$. From equation 4.30 it follows that:

$$\rho_{0,0} = 1 - \rho_{1,1} - \rho_{-1,-1}. \quad (4.31)$$

This construction can be used to highlight the difference between polarization and spin-alignment by using a very simple example, namely assuming that $\rho_{1,1} = \rho_{-1,-1} \neq 1/3$. It follows that $\rho_{0,0} = 1 - 2\rho_{1,1} \neq \rho_{1,1}$. In this scenario there is a preferred spin-alignment but since the projections along the positive or negative spin axis are equal there is no net-polarization. This means that the spin-alignment does not imply polarization. In the case of no net-polarization of a spin 1 particle, i.e. $\rho_{1,1} = \rho_{-1,-1}$, it can be shown

(details in [34] and [35]) that the function:

$$W(\vartheta) = \frac{3}{4} [1 - \rho_{00} + (3\rho_{00} - 1)\cos^2\vartheta] \quad (4.32)$$

describes the yield of the investigated particle. If the vector meson decays into two daughter particles, then ϑ is the angle between the momentum of the vector meson in the laboratory system and the momentum of one of its daughter particles in the rest system of the parent particle. This can be applied to the K^{*+} decay into $K_S^0 + \pi^+$. Hence the coefficient ρ_{00} of K^{*+} can be extracted from the data by repeating the analysis presented in section 4.3, only this time the differential analysis needs to be performed by using the observable $\cos\vartheta_{K_S^0}$ and fitting the resulting corrected spectrum with the function $W(\vartheta_{K_S^0})$. Here the observable ϑ is replaced by the angle between the K^{*+} and K_S^0 particles. The choice is arbitrary, without loss of generality the angle between K^{*+} and π^+ could have been used. The resulting corrected IMS from this procedure is shown in figure 4.21. The result for ρ_{00} is:

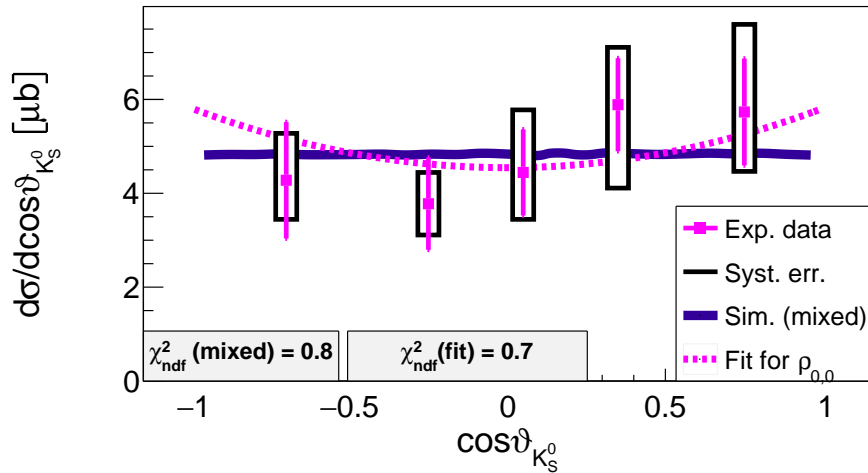


FIGURE 4.21: Corrected $\cos\vartheta_{K_S^0}$ IMS of K^{*+} . The estimation of the systematical uncertainties (see fig. 4.22) are calculated in analogy to all corrected IM spectra presented in section 4.3.

$$\rho_{00} = 0.39 \pm 0.09(\text{stat})_{-0.09}^{+0.10}(\text{syst}). \quad (4.33)$$

This value is compatible with the case of no spin-alignment. Nevertheless the relatively large uncertainties cannot completely exclude the possibility for a preferred spin-orientation.

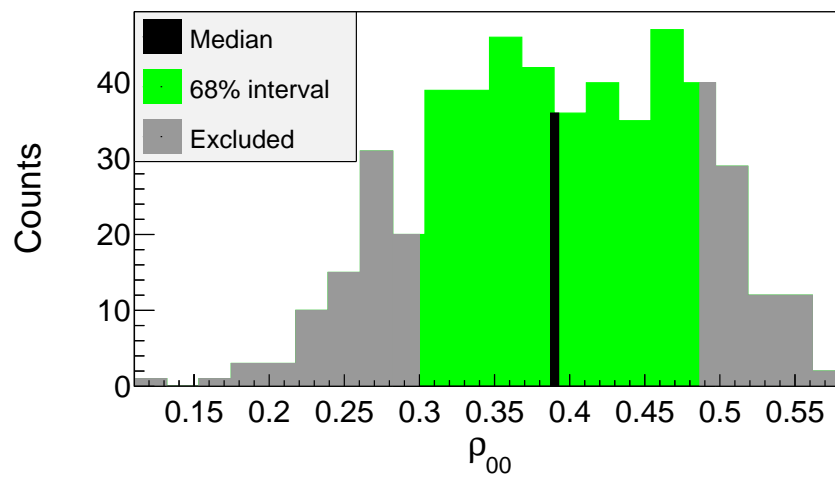


FIGURE 4.22: Calculation of the systematic uncertainty of ρ_{00} . The median value is 0.39, the 68% confidence interval is [0.30, 0.49]

Chapter 5

Summary and conclusions

The HADES experiment provided a great opportunity to investigate an unexplored energy region regarding the production of the $K^*(892)^+$ particle. The performed analysis, the results of which were published in Physical Review C [6], revealed that the two main contributing production channels are $p + p \rightarrow p + \Lambda + K^{*+}$ and $p + p \rightarrow N + \Sigma + K^{*+}$. The contribution of the latter channel has been estimated to be:

$$p^{(\Sigma)} = 0.41^{+0.19}_{-0.22}.$$

The total production cross section of $K^*(892)^+$ was calculated to be:

$$\sigma_{\text{tot}}(K^*(892)^+) = 9.5 \pm 0.9(\text{stat})^{+1.1}_{-0.9}(\text{syst}) \mu\text{b}.$$

Figure 5.1 shows how this result relates to the existing world data. The new result follows the trend observed in the data so far. The fit to the K^{*+} data can be used for extrapolating the total production cross section of the particle down to an excess energy of only 231 MeV. The obtained result will be able to provide valuable input for transport models as well as to serve as a reference for future studies of K^{*+} production in proton-nucleus and heavy-ion collisions. For example, this result can help analyzing the p-Nb HADES data, recorded at exactly the same beam energy, which will provide information about the cold nuclear matter effects influencing the production of the K^{*+} particle.

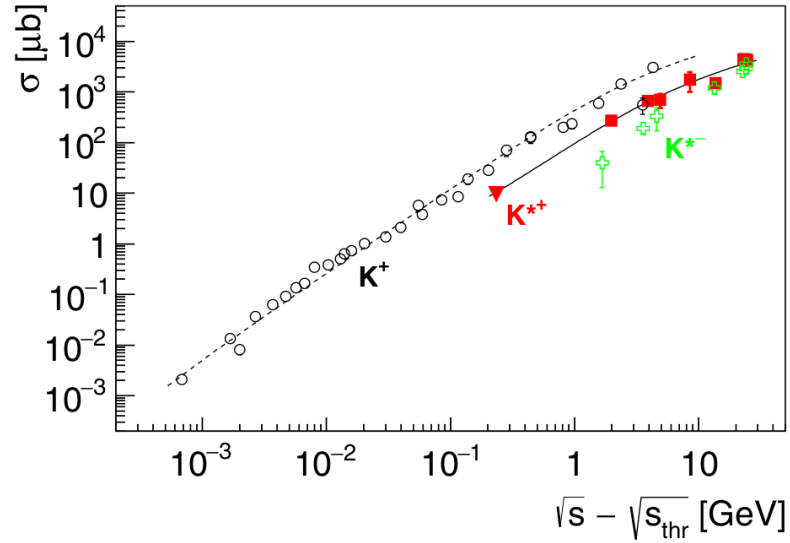


FIGURE 5.1: Energy ($\sqrt{s} - \sqrt{s_{thr}}$) dependence of the total cross section for the processes: i) $pp \rightarrow K^*(892)^+ X$ (squares — world data [19, 36–38], triangle — present work), ii) $pp \rightarrow K^*(892)^- X$ (empty crosses), and iii) $pp \rightarrow K^+ X$ (empty circles) ([39–41] and references therein). The solid (dashed) line is a fit to the $K^*(892)^+$ (K^+) data with $f(x) = C(1 - (D/x)^\mu)^\nu$, where $x = \sqrt{s}$. The numerical values are $C = 3.22 \times 10^6(1.04 \times 10^5)$, $D = 2.89(2.55)$ GeV, $\mu = 1.19 \times 10^{-2}(1.16 \times 10^{-1})$, $\nu = 1.86(1.67)$ [6].

The method used to extract the cross section provided an opportunity to obtain information regarding the spin-alignment properties of the K^{*+} production. The result

$$\rho_{00} = 0.39 \pm 0.09(\text{stat})_{-0.09}^{+0.10}(\text{syst})$$

cannot conclusively exclude the hypothesis for a spin-alignment. It is however fully compatible with the no spin alignment case ($\rho_{00} = 0.33$) and does not show any significant hint about a possible deviation.

Appendix A

Neutral kaons

Below I summarize the text that can be found in section 4.4.3.1 of the book “Introduction to Elementary Particles” by David Griffiths [10].

Using the CP operator one can define two distinct CP eigenstates:

$$|K_1\rangle = \left(\frac{1}{\sqrt{2}}\right) (|K^0\rangle - |\bar{K}^0\rangle) \quad \text{and} \quad |K_2\rangle = \left(\frac{1}{\sqrt{2}}\right) (|K^0\rangle + |\bar{K}^0\rangle), \quad (\text{A.1})$$

with

$$\text{CP} |K_1\rangle = |K_1\rangle \quad \text{and} \quad \text{CP} |K_2\rangle = -|K_2\rangle, \quad (\text{A.2})$$

where K^0 and \bar{K}^0 correspond to the neutral kaon and antikaon. It can be shown that under the assumption that CP is conserved, K_1 should always decay into two pions, while K_2 into three:

$$K_1 \rightarrow \pi^+ + \pi^- \quad \text{or} \quad K_1 \rightarrow \pi^0 + \pi^0, \quad (\text{A.3})$$

$$K_2 \rightarrow \pi^+ + \pi^- + \pi^0 \quad \text{or} \quad K_2 \rightarrow \pi^0 + \pi^0 + \pi^0. \quad (\text{A.4})$$

The energy released in the 2π decays is greater and therefore the decay is faster. However it was proven that K_2 can in fact decay into two pions. This may happen because of the CP violation in weak decays. Let us define K_S^0 and K_L^0 as the short- and long-lived states respectively:

$$|K_S^0\rangle = \frac{1}{\sqrt{1+|\epsilon|^2}} (|K_1\rangle + \epsilon |K_2\rangle), \quad (\text{A.5})$$

$$|K_L^0\rangle = \frac{1}{\sqrt{1+|\epsilon|^2}} (|K_2\rangle + \epsilon |K_1\rangle). \quad (\text{A.6})$$

Obviously both the short- and long-lived states can decay into all possible channels. However, since the coefficient ϵ is very small, most of K_S^0 decay into 2 pions and most of K_L^0 decay into 3 pions. An anomaly related to the CP violation happens only in roughly 1 in 500 events. Additionally, since the c_τ value¹ of K_S^0 and K_L^0 are 2.68 cm and 15.34 m respectively, most of the K_S^0 particles and only a fraction of the K_L^0 particles, will decay inside the HADES detector. Thus it is absolutely reasonable to neglect any effects of the CP violation and to assume that the reconstructed neutral kaons are only K_S^0 particles and the number of K_L^0 and K_S^0 particles is the same.

¹ c_τ is the speed of light multiplied by the mean life time τ and represents the mean distance a particle would travel before it decays, assuming that it is traveling at the speed of light.

Appendix B

Phase space effects on the spectral shape

Low-mass minimum

The PLUTO simulation of the K^{*+} IMS (fig. 4.6) clearly visualizes that there is a zero yield for masses below c.a. 637 MeV. This is related to the decay of K^{*+} into K_S^0 and π^+ , the reaction that we exclusively reconstruct. The requirement this reaction to happen is the mass of the mother particle, K^{*+} in our example, to be equal or greater than the sum of the masses of the two daughter particles. This can be shown mathematically using four-vectors as follows:

$$\begin{aligned} P_{K^{*+}} &= P_{K_S^0} + P_{\pi^+} \\ P_{K^{*+}}^2 &= P_{K_S^0}^2 + P_{\pi^+}^2 + 2 \cdot P_{K_S^0} \cdot P_{\pi^+} \\ m_{K^{*+}}^2 &= m_{K_S^0}^2 + m_{\pi^+}^2 + 2 \cdot \left[E_{K_S^0} \cdot E_{\pi^+} - \vec{p}_{K_S^0} \cdot \vec{p}_{\pi^+} \right]. \end{aligned} \quad (\text{B.1})$$

We can, without loss of generality, observe the system in the rest frame of K^{*+} , i.e.

$$\begin{aligned} \vec{p}_{K^{*+}} &= \vec{p}_{K_S^0} + \vec{p}_{\pi^+} = 0, \\ \vec{p}_{K_S^0} &= -\vec{p}_{\pi^+} = \vec{p}. \end{aligned} \quad (\text{B.2})$$

Combining equations B.1 and B.2 we obtain:

$$m_{K^{*+}}^2 = m_{K_S^0}^2 + m_{\pi^+}^2 + 2 \cdot \left[E_{K_S^0} \cdot E_{\pi^+} + |\vec{p}|^2 \right].$$

Using the general relation

$$E^2 = m^2 + p^2 \quad (\text{B.3})$$

we obtain

$$m_{K^{*+}}^2 = m_{K_S^0}^2 + m_{\pi^+}^2 + 2 \cdot \left[\sqrt{m_{K_S^0}^2 + |\vec{p}|^2} \cdot \sqrt{m_{\pi^+}^2 + |\vec{p}|^2} + |\vec{p}|^2 \right]. \quad (\text{B.4})$$

The term in the brackets is always positive and it is minimal when $|\vec{p}| = 0$. In that case

$$\begin{aligned} (m_{K^{*+}}^2)_{\min} &= m_{K_S^0}^2 + m_{\pi^+}^2 + 2 \cdot m_{K_S^0} \cdot m_{\pi^+} = \left(m_{K_S^0} + m_{\pi^+} \right)^2, \\ \Rightarrow (m_{K^{*+}})_{\min} &= m_{K_S^0} + m_{\pi^+} \approx (497.6 + 139.6) \text{ MeV} = 637.2 \text{ MeV}. \end{aligned} \quad (\text{B.5})$$

High-mass maximum

The cut-off visible in the simulated IM spectrum (figures 4.6 and 4.7) is due to the limited excess energy of the reaction. For the full data it is quite straightforward to understand that the maximum invariant mass of K^{*+} is:

$$\{\text{IM}_{K^{*+}}\}_{\max} = M(K^{*+}) + \varepsilon. \quad (\text{B.6})$$

This relation follows directly from the energy conservation (eq. 2.10 and 2.11) and the definition of the excess energy (eq. 1.2) under the assumption that the momentum of K^{*+} is zero. However if there is a certain restriction regarding the momentum of K^{*+} then it is a bit more difficult to obtain an analytic solution for the maximum allowed $\text{IM}_{K^{*+}}$ value. Let us examine the situation when there is a minimum allowed momentum p_{cut} of K^{*+} . The total energy of the system is

$$\sqrt{s} = E_{\text{tot}} = E_p + E_\Lambda + E_{K^{*+}}. \quad (\text{B.7})$$

The maximum $\text{IM}_{K^{*+}}$ corresponds to a maximal $E_{K^{*+}}$. This, on the other hand, enforces:

$$\min \{E_p + E_\Lambda\} = \min \left\{ \sqrt{m_p^2 + p_p^2} + \sqrt{m_\Lambda^2 + p_\Lambda^2} \right\}, \quad (\text{B.8})$$

and thus

$$\max \{E_{K^{*+}}\} = E_{\text{tot}} - \min \left\{ \sqrt{m_p^2 + p_p^2} + \sqrt{m_\Lambda^2 + p_\Lambda^2} \right\}. \quad (\text{B.9})$$

The conservation of momentum demands

$$p_{\text{cut}} = p_p + p_\Lambda, \quad (\text{B.10})$$

therefore B.9 transforms in

$$\max \{E_{K^{*+}}\} = E_{\text{tot}} - \min \left\{ \sqrt{m_p^2 + p_p^2} + \sqrt{m_\Lambda^2 + (p_p - p_{\text{cut}})^2} \right\} \quad (\text{B.11})$$

Let's apply a simple first-derivation search for an extremum with respect to p_p :

$$\frac{p_p}{\sqrt{m_p^2 + p_p^2}} + \frac{p_p - p_{\text{cut}}}{\sqrt{m_\Lambda^2 + (p_p - p_{\text{cut}})^2}} = 0, \quad (\text{B.12})$$

$$\Rightarrow \frac{p_p^2}{m_p^2 + p_p^2} = \frac{(p_p - p_{\text{cut}})^2}{m_\Lambda^2 + (p_p - p_{\text{cut}})^2}, \quad (\text{B.13})$$

$$\Leftrightarrow p_p^2 m_\Lambda^2 + \cancel{p_p^2 (p_p - p_{\text{cut}})^2} = m_p^2 (p_p - p_{\text{cut}})^2 + \cancel{p_p^2 (p_p - p_{\text{cut}})^2}, \quad (\text{B.14})$$

$$\Leftrightarrow p_p^2 m_\Lambda^2 - m_p^2 (p_p^2 + p_{\text{cut}}^2 - 2p_p p_{\text{cut}}) = 0, \quad (\text{B.15})$$

$$\Leftrightarrow p_p^2 (m_\Lambda^2 - m_p^2) + 2p_p p_{\text{cut}} m_p^2 - p_{\text{cut}}^2 m_p^2 = 0 \quad (\text{B.16})$$

The last expression can be easily solved using the standard solution of a quadratic equation:

$$p_p = \frac{-p_{\text{cut}} m_p^2 \pm \sqrt{\cancel{p_{\text{cut}}^2 m_p^4} + (m_\Lambda^2 - \cancel{m_p^2}) p_{\text{cut}}^2 m_p^2}}{m_\Lambda^2 - m_p^2} \quad (\text{B.17})$$

$$\xrightarrow{p_p > 0} p_p = \frac{-p_{\text{cut}} m_p^2 + p_{\text{cut}} m_p m_\Lambda}{m_\Lambda^2 - m_p^2} = p_{\text{cut}} \frac{m_p m_\Lambda - m_p^2}{m_\Lambda^2 - m_p^2}. \quad (\text{B.18})$$

All parameters in the above equation are known. In the case of $p_{\text{cut}} = 470$ MeV (see fig. 4.7)

$$\Rightarrow p_p = 214.7 \text{ MeV}. \quad (\text{B.19})$$

The maximum $\text{IM}_{K^{*+}}$ can be obtained by using the property B.3:

$$\max \{E_{K^{*+}}\} = \sqrt{\max \{\text{IM}_{K^{*+}}\}^2 + p_{\text{cut}}^2}, \quad (\text{B.20})$$

$$\Rightarrow \max \{\text{IM}_{K^{*+}}\} = \sqrt{\max \{E_{K^{*+}}\}^2 - p_{\text{cut}}^2}. \quad (\text{B.21})$$

Using the value of $p_{\text{cut}} = 470$ MeV and combining equations B.11, B.19 and B.21 one obtains:

$$\max \{IM_{K^{*+}}\} \approx 960 \text{ MeV}. \quad (\text{B.22})$$

Appendix C

Number of simulated events

An important parameter for the simulation is the number of events needed. The efficiency of the reconstruction is between 1/200 and 1/100, depending on the phase-space region. According to the “rule of thumb” an efficiency of 1/150 is assumed in the following calculations. As shown in the present work, the available experimental K^{*+} yield is around 1500. Initially the simulated PLUTO yield was 2M events. This resulted in roughly 13k K^{*+} candidates after running HGeant. Since the error goes down as the square root of the number of events, this means that the ratio between the uncertainty in the simulation and in the experiment is only $\sqrt{13000/1500} \approx 2.9$. The desired goal was to achieve a smaller uncertainty related to the simulation, thus the PLUTO sample was increased to 16Mi= $2^{24} \approx 16.8$ M. This exact number was chosen because: a) the CPU time was still reasonable (a total of a few hundred hours distributed on more than 50 units) b) this ensures that only 10% of the uncertainty is related to the simulation. c) I really like numbers that are powers of 2. It should be noted that this huge number of events brings another issue with it: when accessing the PLUTO data for the AEC 16Mi of iterations are needed in order to go through all events. Since the post-analysis was performed on local machines (like my personal laptop or desktop) this slowed significantly down the analysis. However the simulation error discussed so far is related to the limited HGeant statistics, which is so low due to the acceptance and efficiency effects. The PLUTO sample is not influenced by that and hence the error related to PLUTO is a factor of $\sqrt{150} \approx 12$ times less than compared to HGeant. Therefore I have decided to reduce the number of events accessed from the PLUTO sample to 2M. This still ensures that the PLUTO error is a factor of 4.2 smaller than

the HGeant error and a factor of 36.5 smaller than the experimental error. This scaling introduces discrepancy to the AE correction factor, which is obtained using the ratio between the yield of the PLUTO and HGeant samples, hence the values and errors of one of the samples needed to be scaled accordingly. WLOG it was chosen to scale down the HGeant yield (and errors) by a factor of $2^{24}/(2 \cdot 10^6) \approx 8.4$. For this reason in section 4.3.4.1 the number 2M was used when normalizing the number of events used by the two-channel model.

Appendix D

Uncorrected spectra

Below all uncorrected spectra obtained during the analysis are plotted.

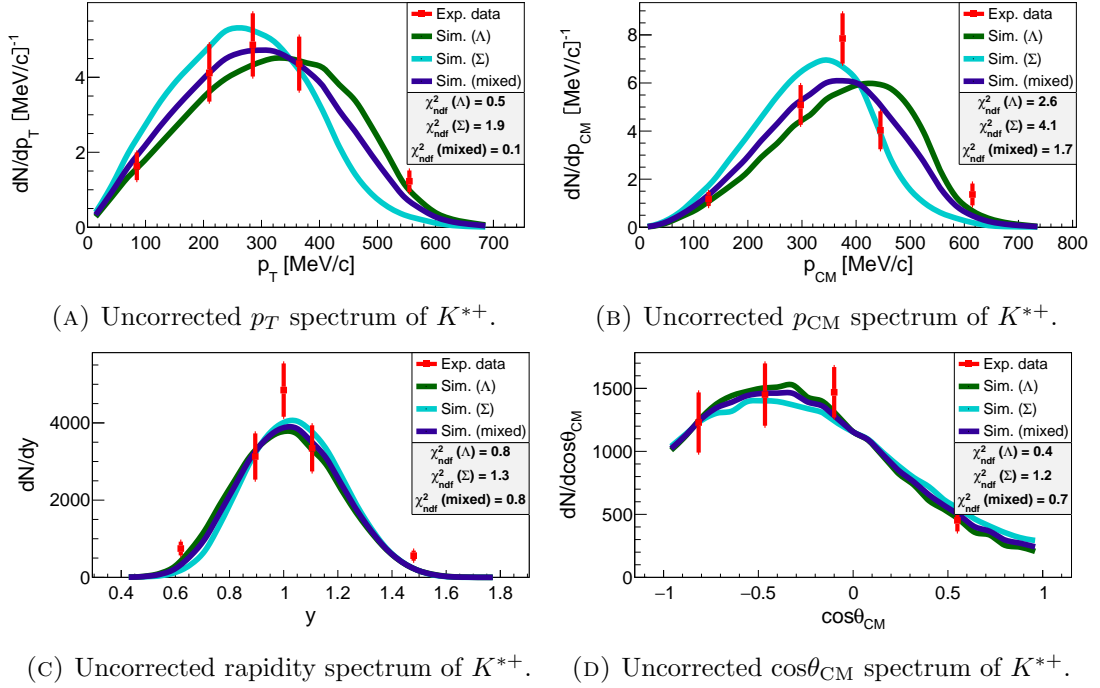


FIGURE D.1: All uncorrected spectra of K^{*+} . The expected values, as obtained from the HGeant output, are plotted on the top of the experimental data. The three different curves represent different Σ -channel contributions. The value of $p^{(\Sigma)}$ for the two-channel model is different for each curve, the values used are the best fit for each observable (see 4.19). The total yield of each model is normalized to the total experimental yield.

Appendix E

Conditions regarding the quality assurance

The following section provides further information regarding the conditions listed in table 4.8.

- **Failing to fit the yield in a certain bin**

Sometimes it is possible to have a fit failure. This happens quite often in the experimental data in the bins with least room in the phase space. If a single bin fails to be properly fitted the yield is extrapolated based on the HGeant simulation. This is achieved by normalizing the yield in the problematic bin from HGeant to the experimental data by using the total yield from all other bins as a reference. If the fitting procedure failed in multiple bins, the whole set of topological cuts is rejected.

- **Global fit**

The fitting procedure was set up in a way that allowed to fit all of the bins simultaneously, for example by demanding that the mass should always be the same in all bins. However since many of the fit parameters were fixed, this procedure was found to bring no significant improvement and all bins were fitted independently. Even so the fitting procedure still provided as an output a global covariance matrix and a p-value, i.e. taking all bins into account. These observables were used in the conditions for the topological cuts (see table 4.8).

Appendix F

Legendre polynomials

The Legendre polynomials are defined as follows [42, 43]:

$$\begin{aligned} P_n(x) &= \frac{1}{2^n} \sum_{k=0}^n \binom{n}{k}^2 (x-1)^{n-k} (x+1)^k \\ &= \sum_{k=0}^n \binom{n}{k} \binom{-n-1}{k} \left(\frac{1-x}{2}\right)^k \\ &= 2^n \cdot \sum_{k=0}^n x^k \binom{n}{k} \binom{\frac{n+k-1}{2}}{n}. \end{aligned} \tag{F.1}$$

In figure 4.20d the spectrum is fitted with a combination of $P_0(x)$ and $P_2(x)$, i.e.

$$P_{0,2}(x) = a_0 P_0(x) + a_2 P_2(x) = a_0 + \frac{a_2}{2} (3x^2 - 1). \tag{F.2}$$

This function is symmetric around 0, just as the $\cos\theta_{CM}$ observable, which is why $P_{0,2}(x)$ was used to fit the spectrum. An isotropic production of the K^{*+} particle corresponds to the result from the PLUTO simulation (the purple line in figure 4.20d), which is a rather flat distribution. The function F.2 should be a better fit to the data in the case of a strongly anisotropic K^{*+} production.

Bibliography

- [1] G. Agakishiev et al. Deep sub-threshold $K^*(892)^0$ production in collisions of Ar + KCl at 1.76-A-GeV. *Eur. Phys. J.*, A49:34, 2013. doi: 10.1140/epja/i2013-13034-7. URL <http://dx.doi.org/10.1140/epja/i2013-13034-7>.
- [2] Johannes Siebenson and Laura Fabbietti. Investigation of the $\Lambda(1405)$ line shape observed in pp collisions. *Phys. Rev.*, C88:055201, 2013. doi: 10.1103/PhysRevC.88.055201. URL <http://link.aps.org/doi/10.1103/PhysRevC.88.055201>.
- [3] G. Agakishiev et al. Medium effects in proton-induced K^0 production at 3.5 GeV. *Phys. Rev.*, C90:054906, 2014. doi: 10.1103/PhysRevC.90.054906. URL <http://link.aps.org/doi/10.1103/PhysRevC.90.054906>.
- [4] G. Agakishiev et al. Associate K^0 production in p+p collisions at 3.5 GeV: The role of $\Delta(1232)^{++}$. *Phys. Rev.*, C90:015202, 2014. doi: 10.1103/PhysRevC.90.015202. URL <http://link.aps.org/doi/10.1103/PhysRevC.90.015202>.
- [5] G. Agakishiev et al. Partial Wave Analysis of the Reaction $p(3.5\text{GeV}) + p \rightarrow pK^+\Lambda$ to Search for the " ppK^- " Bound State. *Phys. Lett.*, B742:242–248, 2015. doi: 10.1016/j.physletb.2015.01.032. URL <http://www.sciencedirect.com/science/article/pii/S0370269315000428>.
- [6] G. Agakishiev et al. $K^*(892)^+$ production in proton-proton collisions at $E_{beam} = 3.5$ GeV. *Phys. Rev.*, C92(2):024903, 2015. doi: 10.1103/PhysRevC.92.024903. URL <http://link.aps.org/doi/10.1103/PhysRevC.92.024903>.
- [7] K. A. Olive et al. Review of Particle Physics. *Chin. Phys.*, C38:090001, 2014. doi: 10.1088/1674-1137/38/9/090001. URL <http://stacks.iop.org/1674-1137/38/i=9/a=090001>.

- [8] J. Beringer et al. Review of Particle Physics (RPP). *Phys. Rev.*, D86:010001, 2012. doi: 10.1103/PhysRevD.86.010001. URL <http://link.aps.org/doi/10.1103/PhysRevD.86.010001>.
- [9] Wikipedia - Kaon. <https://en.wikipedia.org/wiki/Kaon#Mixing>, . Accessed: 2016-04-06.
- [10] David Griffiths. *Introduction to Elementary Particles*. WILEY-VCH, 2008.
- [11] GeoGebra. <http://www.geogebra.org/>. Accessed: 2016-03-23.
- [12] Mark Thomson. *Modern particle physics*. Cambridge University Press, 2013.
- [13] Y. Aoki, G. Endrodi, Z. Fodor, S. D. Katz, and K. K. Szabo. The Order of the quantum chromodynamics transition predicted by the standard model of particle physics. *Nature*, 443:675–678, 2006. doi: 10.1038/nature05120. URL <http://www.nature.com/nature/journal/v443/n7112/full/nature05120.html>.
- [14] Pedro Bicudo, Nuno Cardoso, and Marco Cardoso. The Chiral crossover, static-light and light-light meson spectra, and the deconfinement crossover. *PoS, BORMIO2011:062*, 2011. URL <https://arxiv.org/abs/1105.0063>.
- [15] C. Markert, G. Torrieri, and Johann Rafelski. Strange Hadron Resonances: Freeze-Out Probes in HeavyIon Collisions. *AIP Conf. Proc.*, 631:533–552, 2002. doi: 10.1063/1.1513698. URL <http://scitation.aip.org/content/aip/proceeding/aipcp/10.1063/1.1513698>.
- [16] A. G. Knospe. Resonances as Probes of Heavy-Ion Collisions at ALICE. *J. Phys. Conf. Ser.*, 612(1):012064, 2015. doi: 10.1088/1742-6596/612/1/012064. URL <http://stacks.iop.org/1742-6596/612/i=1/a=012064>.
- [17] C. M. Ko, Z. G. Wu, L. H. Xia, and G. E. Brown. Effect of chiral restoration on kaon production in relativistic heavy ion collisions. *Phys. Rev. Lett.*, 66:2577–2580, 1991. doi: 10.1103/PhysRevLett.66.2577. URL <http://link.aps.org/doi/10.1103/PhysRevLett.66.2577>. [Erratum: *Phys. Rev. Lett.*67,1811(1991)].
- [18] Kazuo Tsushima, Alexander Sibirtsev, and Anthony William Thomas. Strangeness production from πN collisions in nuclear matter. *Phys. Rev.*, C62:064904, 2000. doi: 10.1103/PhysRevC.62.064904. URL <http://link.aps.org/doi/10.1103/PhysRevC.62.064904>.

- [19] K. Böckmann et al. Inclusive $K^{*\pm}(892)$ Production in pp and π^+p Interactions. *Nucl. Phys. B*, 166:284, 1980. doi: 10.1016/0550-3213(80)90228-X. URL <http://www.sciencedirect.com/science/article/pii/055032138090228X>.
- [20] C. Sturm and H. Stöcker. The facility for antiproton and ion research fair. *Physics of Particles and Nuclei Letters*, 8(8):865–868, 2011. ISSN 1531-8567. doi: 10.1134/S1547477111080140. URL <http://dx.doi.org/10.1134/S1547477111080140>.
- [21] K. Lapidus et al. The HADES-at-FAIR project. *Phys. Atom. Nucl.*, 75:589–593, 2012. doi: 10.1134/S1063778812050146. URL <http://dx.doi.org/10.1134/S1063778812050146>.
- [22] Jaroslav Adam et al. Production of light nuclei and anti-nuclei in pp and $Pb-Pb$ collisions at energies available at the CERN Large Hadron Collider. *Phys. Rev.*, C93(2):024917, 2016. doi: 10.1103/PhysRevC.93.024917. URL <http://link.aps.org/doi/10.1103/PhysRevC.93.024917>.
- [23] GEometry ANd Tracking - GEANT. <http://www.geant4.org/geant4/>. Accessed: 2016-03-19.
- [24] G. Agakishiev et al. The High-Acceptance Dielectron Spectrometer HADES. *Eur. Phys. J.*, A41:243–277, 2009. doi: 10.1140/epja/i2009-10807-5. URL <http://dx.doi.org/10.1140/epja/i2009-10807-5>.
- [25] NPI Rez group - HADES. <http://ojs.ujf.cas.cz/ionty/hades/>. Accessed: 2016-03-20.
- [26] K. Lapidus et al. Dielectron production in pp and dp collisions at 1.25-GeV/u with HADES. In *19th International Baldin Seminar on High Energy Physics Problems: Relativistic Nuclear Physics and Quantum Chromodynamics (ISHEPP 2008) Dubna, Russia, September 29-October 4, 2008*, 2009. URL <http://inspirehep.net/record/817478/files/arXiv:0904.1128.pdf>.
- [27] ROOT. <https://root.cern.ch/>. Accessed: 2016-03-21.
- [28] I. Frohlich et al. Pluto: A Monte Carlo Simulation Tool for Hadronic Physics. *PoS, ACAT2007:076*, 2007. URL <https://arxiv.org/abs/0708.2382>.
- [29] HGeant. <https://www-hades.gsi.de/?q=computing>. Accessed: 2016-03-20.

- [30] G. Agakishiev et al. Inclusive dielectron spectra in p+p collisions at 3.5 GeV. *Eur. Phys. J.*, A48:64, 2012. doi: 10.1140/epja/i2012-12064-y. URL <http://dx.doi.org/10.1140/epja/i2012-12064-y>.
- [31] Jia-Chii Berger-Chen. *The Production of K^0 in p+p Reactions at 3.5 GeV - Inclusive and Exclusive Studies with the HADES Detector*. PhD thesis, Technical University of Munich, 2015.
- [32] Jia-Chii Berger-Chen, Laura Fabbietti, and Kirill Lapidus. Neutral kaon production in p+p and p+Nb collisions. *Hyperfine Interact.*, 210:111–114, 2012. doi: 10.1007/s10751-012-0595-6. URL <http://dx.doi.org/10.1007/s10751-012-0595-6>.
- [33] C. Bourrely, E. Leader, and J. Soffer. Polarization phenomena in hadronic reactions. *Physics Reports*, 59(2):95 – 297, 1980. ISSN 0370-1573. doi: [http://dx.doi.org/10.1016/0370-1573\(80\)90017-4](http://dx.doi.org/10.1016/0370-1573(80)90017-4). URL <http://www.sciencedirect.com/science/article/pii/0370157380900174>.
- [34] John F. Donoghue. Hadronic polarization in neutrino scattering. *Phys. Rev. D*, 17:2922–2926, Jun 1978. doi: 10.1103/PhysRevD.17.2922. URL <http://link.aps.org/doi/10.1103/PhysRevD.17.2922>.
- [35] A. Chukanov et al. Production properties of $K^*(892)^\pm$ vector mesons and their spin alignment as measured in the NOMAD experiment. *Eur. Phys. J.*, C46:69–79, 2006. doi: 10.1140/EPJC/S2006-02500-4. URL <http://dx.doi.org/10.1140/epjc/s2006-02500-4>.
- [36] M. Yu. Bogolyubsky, V.A. Bumazhnov, A.E. Kiryunin, A.I. Kotova, M.S. Levitsky, et al. Study of Neutral Strange Particle Production in pp Interactions at 32-GeV/c and Comparison With $\bar{p}p$ Data. *Sov. J. Nucl. Phys.*, 50:424, 1989.
- [37] D. Brick, H. Rudnicka, A.M. Shapiro, M. Widgoff, R.E. Ansorge, et al. Inclusive Strange Resonance Production in pp , π^+p and K^+p Interactions at 147-GeV/c. *Phys. Rev. D*, 25:2248–2258, 1982. doi: 10.1103/PhysRevD.25.2248. URL <http://link.aps.org/doi/10.1103/PhysRevD.25.2248>.
- [38] T. Aziz et al. Inclusive K^* and Σ^* Production in 360-GeV/c pp Interactions Using the European Hybrid Spectrometer. *Z. Phys. C*, 30:381, 1986. doi: 10.1007/BF01557601. URL <http://dx.doi.org/10.1007/BF01557601>.

- [39] M. Abdel-Bary et al. Production of Λ and Σ^0 hyperons in proton-proton collisions. *Eur. Phys. J.*, A46:27–44, 2010. doi: 10.1140/epja/i2010-11023-0,10.1140/epja/i2010-11062-5. URL <http://dx.doi.org/10.1140/epja/i2010-11023-0>. [Erratum: *Eur. Phys. J.*A46,435(2010)].
- [40] M. Abdel-Bary et al. The $pp \rightarrow nK^+\Sigma^+$ reaction at 2.95 GeV/c. *Eur. Phys. J.*, A48:37, 2012. doi: 10.1140/epja/i2012-12037-2. URL <http://dx.doi.org/10.1140/epja/i2012-12037-2>.
- [41] J.T. Reed, A.C. Melissinos, N.W. Reay, T. Yamanouchi, E.J. Sacharidis, et al. Production of K^+ Mesons in 2.85- and 2.40-BeV p-p Collisions. *Phys. Rev.*, 168: 1495–1508, 1968. doi: 10.1103/PhysRev.168.1495. URL <http://link.aps.org/doi/10.1103/PhysRev.168.1495>.
- [42] Kevin Cahill. *Physical Mathematics*. Cambridge University Press, 2013.
- [43] Wikipedia - Legendre Polynomials. https://en.wikipedia.org/wiki/Legendre_polynomials, . Accessed: 2016-04-10.